Decision Making Under Uncertainty by Trustworthy Dynamic Bayesian Networks for Severe Accident Management in Nuclear Power Plants

Giovanni Roma[1], Francesco Di Maio[1*], Enrico Zio[1,2]

1 Energy Department, Politecnico di Milano, Via La Masa 34, Milano, 20156, Italy.

[2]MINES Paris-PSL University, CRC, Sophia Antipolis, France

* Corresponding author: francesco.dimaio@polimi.it

Abstract

Severe Accident Management (SAM) of a Nuclear Power Plant (NPP) relies on a set of actions to mitigate the consequences of severe accidents, and recover its safe and stable state. Dynamic Bayesian Networks (DBNs) can support decision-making during accident progression and, thus, serve as Accident Management Support Tools (AMSTs).

In this work, we propose a methodological framework for quantifying, in real-time, the uncertainty of the output of a DBN-based AMST to enable trustworthy decision-making with regards to the selection of the best action to mitigate the developing accident scenario. The proposed methodology is exemplified on a Loss of Coolant Accident (LOCA) in a WWER-1000 nuclear reactor. Results show that accounting for the uncertainty of the output of the DBN enables a reliable and robust selection of the proper mitigative actions to avoid severe consequences, ultimately strengthening the support for safe accident management decisions.

Keywords: Nuclear power plants (NPPs), Severe accident management (SAM), Severe accident management guidelines (SAMGs), Accident management support tools (AMSTs), Decision making, Dynamic Bayesian network (DBN), WWER-1000, Loss of coolant accident (LOCA).

Acronyms

AICC	Adiabatic Isocoric Complete Combustion
AMST	Accident Management Support Tool
ANN	Artificial Neural Network
BN	Bayesian Network
BT	Bow-Tie
CB	Containment Building
CCFP	Conditional Containment Failure Probability
CDF	Core Damage Frequency
CPT	Conditional Probability Table
CRA	Computational Risk Assessment
DBN	Dynamic Bayesian Network
DPRA	Dynamic Probabilistic Risk Assessment
EF	Equal Frequency
EPIS	Estimated Posterior Importance Sampling
FCV	Filtered Containment Venting
FT	Fault Tree
FTN	Fuzzy Triangular Number
HPIS	High-Pressure Injection System
IE	Initiating Event
LERF	Large Early Release Frequency
LOCA	Loss of Coolant Accident
MAP	Maximum A Posteriori
MC	Monte Carlo
MFM	Multilevel Flow Modeling
MLE	Maximum Likelihood Estimation
NPP	Nuclear Power Plant
NRC	Nuclear Regulatory Commission
PDS	Plant Damage State
POCs	Plant Operating Conditions
SAM	Severe Accidents Management
SAMGs	Severe Accident Management Guidelines
TH	Thermal Hydraulic
TSC	Technical Support Center
WWER	Water-Water Energetic Reactor

List of symbols

Symbols	Dimension	Description
k	1×1	Current time step (i.e., the one at which the monitored data are available)
i	1×1	Generic future time step (i.e., $i > k$)
T	1×1	Last time step
Δt	1×1	Time interval between two successive time steps
p	1×1	Number of static observable variables
q	1×1	Number of static hidden variables
r	1×1	Number of dynamic hidden variables
s	1×1	Number of dynamic observable variables
Ξ	1×1	Number of risk indices
I	1×1	Number of mitigative safety barriers
$\boldsymbol{\phi}$	$p \times 1$	Vector of static observable variables
$\boldsymbol{\varphi}$	$p \times 1$	Realization of the vector of static observable variables
$\boldsymbol{\Psi}$	$q \times 1$	Vector of static hidden variables
$\boldsymbol{\psi}$	$q \times 1$	Realization of the vector of static hidden variables
$\boldsymbol{X}_{(k)}$	$r \times 1$	Vector of dynamic hidden variables at time step k
ξ	1×1	Index used to identify the ξ^{th} risk index
$\boldsymbol{Y}_{(k)}$	$s \times 1$	Vector of dynamic observable variables at time step k
$\boldsymbol{Z}_{(k)}$	$v \times 1$	Vector of system variable describing the PDS at time step k
$\boldsymbol{M}$	$I \times 1$	Set of the available mitigative safety barriers
N_a	1×1	Number of candidate sequences of actions to be assessed
$\boldsymbol{A}_{(k)}$	$I \times 1$	Vector describing the type of actions carried out by the operator on each mitigative safety barrier at time step k
$A_{l(k)}$	1×1	Variable describing the type of action carried out by the operator on the mitigative safety barrier l at time step k

l	1×1	Index used to identify the l^{th} mitigative safety barrier
$\boldsymbol{A}_{l(0:T)}$	$1 \times (T+1)$	Vector describing the sequence of actions performed on the l^{th} mitigative barrier between 0 and T
Z_n	1×1	Generic n^{th} node of the DBN (i.e., $Z_n \in \{\boldsymbol{\phi}, \boldsymbol{Y}, \boldsymbol{\Psi}, \boldsymbol{X}, \boldsymbol{A}\}$)
$R_{\xi(i)}^{(j)}$	1×1	ξ^{th} risk index at time step $i > k$, computed for action $\boldsymbol{a}_{(k+1:T)}^{(j)}$
γ	1×1	Probability content for the tolerance interval
β	1×1	Confidence level for the tolerance interval
P_{tot}	1×1	Total number of nodes in the BN/DBN
N_{CPT}	1×1	Number of entries of the training data matrix for CPT parameter learning
$\boldsymbol{\mathcal{D}}$	$N_{CPT} \times P_{tot}$	Training data matrix for CPT parameter learning
θ_{nmu}	1×1	CPT parameter for node Z_n, representing $\Pr(Z_n = u \mid Pa(Z_n) = m)$
N_{nmu}	1×1	Number of times the event $(Z_n = u \mid Pa(Z_n) = m)$ is observed in $\boldsymbol{\mathcal{D}}$
α_{nmu}	1×1	Dirichlet prior hyperparameter for θ_{nmu}
c_n	1×1	Cardinality of Z_n (i.e., number of states the node Z_n can take on)
d_n	1×1	Number of combinations the parents of Z_n (i.e., $Pa(Z_n)$) can take on (i.e., $d_n = \prod_{v \in Pa(Z_n)} c_v$)
ϵ_ξ	1×1	Threshold for the ξ^{th} risk index determined by the decision-maker
N_γ^β	1×1	Number of samples needed to ensure the tolerance interval $\left[R_{\xi(i)}^{(j)-}, R_{\xi(i)}^{(j)+}\right]_\gamma^\beta$ satisfies the specified coverage γ and confidence β level
λ	1×1	Index used to identify the λ^{th} decision-making criterion
$\widetilde{W}_\lambda$	1×3	Fuzzy importance weight of the λ^{th} decision criterion with respect to the decision objective;
$\widetilde{W}_{R_\xi}$	1×3	Fuzzy importance weight of the ξ^{th} risk index (sub-criterion) with respect to the *effectiveness*;

$\tilde{S}_{j\lambda}$	1×3	Fuzzy score of alternative $\boldsymbol{a}_{(k+1:T)}^{(j)}$ with respect to the criterion C_λ;
$\tilde{F}_j$	1×3	Overall fuzzy score of alternative $\boldsymbol{a}_{(k+1:T)}^{(j)}$.
T_m	1×1	Mission time: time horizon over which the physical system evolution is considered
$\dot{m}_{BR}(t)$	1×1	Time-dependent flowrate released in the CB from the primary circuit during the accident
r_{BS}	1×1	Break size in the primary circuit
PR_{H2}	1×1	Hydrogen production rate, net of that absorbed by PARs
t_{ign}	1×1	Ignition time of the CB
t_{sp}	1×1	Spray system activation time
$p_{cont}(t)$	1×1	Time-dependent pressure in the CB at time t
$T_{cont}(t)$	1×1	Time-dependent temperature in the CB at time t
$X_{H2O}(t)$	1×1	Time-dependent steam molar fraction in the CB at time t
$X_{H2}(t)$	1×1	Time-dependent hydrogen molar fraction in the CB at time t
$p_{eq,static}$	1×1	Equivalent static pressure load in the CB at $t = t_{ign}$
$C_{regime}(t)$	1×1	Combustion regime that would result from an ignition at time t

1 Introduction

Severe accidents in Nuclear Power Plants (NPPs) are managed through Severe Accident Management Guidelines (SAMGs), which provide a prescriptive set of actions to take for mitigating the consequences and recovering a safe and stable plant state [1]. SAMGs are typically based on a relatively small number of prototypical accident scenarios defined by experts [2]. In addition, Accident Management Support Tools (AMSTs) can be used to assist the decision making during the accident development. AMSTs aim to perform the following tasks: i) prediction of the accident progression, ii) identification of the Plant Damage State (PDS), and iii) support to decisions regarding mitigative and recovery actions. Traditionally AMSTs employ "if-then" rule-based expert systems (e.g., MARS [3], CAMS [4], ADAM [5] and SAMSON [6]), eventually combined with probabilistic and fuzzy logic methods to deal with the uncertainty inherent in expert judgment [7]; however, their development can be quite time-consuming [8]. Recently, Bayesian Networks (BNs) [9] have been used. For example, Groth et al. [10] propose a dynamic risk-informed diagnosis

methodology for accident management, based on BNs whose Conditional Probability Tables (CPTs) are inferred from accident scenarios generated by Dynamic Probabilistic Risk Assessment (DPRA). Roma et al. [11] propose a framework to support NPP severe accident management in NPPs based on Dynamic Bayesian Networks (DBNs) whose CPTs parameters are inferred from accident scenarios generated by Computational Risk Assessment (CRA); Kim et al. [12,13] propose a decision-making framework based on DBNs, whose CPTs parameters are estimated from accidental scenarios generated by the CRA tool RAVEN [14].

However, in BNs and DBNs, the set of accident scenarios considered to infer the CPTs may not fully cover the developing accident scenario, and this uncertainty should be reflected in the CPTs parameters [15] and ultimately in the uncertainty of the outcomes provided by the AMST to support decision making [16].

In this work, we propose a DBN-based AMST [11] for supporting the decisions on the best sequence of mitigative actions to deploy during a severe accident. The proposed AMST: i) assesses the effectiveness of each candidate mitigative action, with respect to limits set by the decision-maker and/or the regulatory body, by predicting user-defined risk indices (e.g., quantitative measures of risk such as the Conditional Containment Failure Probability (CCFP) or the Large Early Release Frequency (LERF)) for the specific scenario developing; ii) estimates the uncertainty of each predicted risk index; iii) indicates the decision (under uncertainty) of the best candidate mitigative action through a fuzzy set theory-based decision-making method of literature [17].

Different works have addressed the issue of quantifying the impact of uncertainties in CPTs of BNs for risk assessment (e.g., through the adoption of Credal Networks [18]) [15,16,19,20]; however, to the authors knowledge, this work is the first to provide the estimate of the uncertainty of DBNs outcomes and consider it pivotal information for the AMST support to decision making for severe accident management under uncertainty.

The remainder of the paper is as follows. Section 2 describes the DBN-based AMST in mathematical terms and formulates the decision-making problem. An application of the proposed framework to a real-world WWER-1000 Nuclear Power Plant (NPP) is presented in Section 3, for which the effectiveness of three alternative actions (i.e., an early, a delayed and a no activation of the spray system) aimed at mitigating the damage to the Containment Building (CB) is evaluated, considering the uncertainty of the DBN-based AMST outcomes for trustworthiness. Section 4 discusses the results. Finally, Section 5 summarizes the findings and concludes the study.

2 The DBN-based AMST

A discrete-time model of the evolution of a severe accident in a NPP is considered, with a finite set of uniformly spaced time steps $[0, 1, 2, \dots, k, \dots, T]$, with duration $\Delta t = t_{k+1} - t_k$. The model is governed by a set of *observable* variables (measurable through sensors or inspections) and *hidden* variables. These

variables can be either *static* (constant over time) or *dynamic* (time-varying). Let us denote the *static observable* variables by $\boldsymbol{\phi} = \left[\phi_1, \dots, \phi_p\right]^T$, the *dynamic observable* variables at time step k by $\boldsymbol{Y}_{(k)} = \left[Y_{1(k)}, \dots, Y_{s(k)}\right]^T$, the *static hidden* variables by $\boldsymbol{\Psi} = \left[\Psi_1, \dots, \Psi_q\right]^T$, and the *dynamic hidden* variables at time step k by $\boldsymbol{X}_{(k)} = \left[X_{1(k)}, \dots, X_{r(k)}\right]^T$. The static observable variables in $\boldsymbol{\phi}$ include, for instance, geometrical and material properties, or the initial operational mode (e.g., power operation, startup, hot/cold shutdown, refueling). Dynamic observable variables $\boldsymbol{Y}_{(k)}$ vary with operational conditions and are continuously monitored (e.g., coolant temperature and radiation levels). Static hidden variables $\boldsymbol{\Psi}$ relate to the IE, the Plant Operating Conditions (POCs), break characteristics (e.g., primary circuit cold leg break size in a LOCA), or constant non-measurable geometrical or material properties. Dynamic hidden variables $\boldsymbol{X}_{(k)}$ cover the Damage State (DS) of non-inspectable safety barriers (e.g., cladding), the magnitude of process events (e.g., air-hydrogen mixture combustion regime: flame acceleration, deflagration, detonation), or non-measurable parameters (e.g., reactor core temperature), which evolve over time and are indirectly inferred from sensor data. At any time step k, the PDS is, thus, defined as a subset of the system variables $\boldsymbol{Z}_{(k)} \subseteq \left[\boldsymbol{\phi}, \boldsymbol{Y}_{(k)}, \boldsymbol{\Psi}, \boldsymbol{X}_{(k)}\right]^T$.

Let $\boldsymbol{M} = [M_1, \dots, M_l, \dots, M_I]^T$ be the list of safety barriers (e.g., containment building spray system, High Pressure Injection System (HPIS)) in place to mitigate the accident escalation, and $\boldsymbol{A}_{(k)} = \left[A_{1(k)}, \dots, A_{l(k)}, \dots, A_{I(k)}\right]^T$ the corresponding actions on $M_1, \dots, M_l, \dots, M_I$ at time step k, namely:

1) $A_{l(k)} = 1$, if M_l is activated at time k (being inactive at $k-1$);
2) $A_{l(k)} = 2$, if M_l is kept inactive at time k (being inactive at $k-1$);
3) $A_{l(k)} = 3$, if M_l is deactivated at time k (being active at $k-1$);
4) $A_{l(k)} = 4$, if M_l is kept active at time k (being active at $k-1$).

Thus, the sequence of actions $\boldsymbol{A}_{(0:T)}$ between the time 0 and k is represented by:

$$\boldsymbol{A}_{(0:T)} = \begin{bmatrix} A_{1(0)} & \cdots & A_{1(T)} \\ \vdots & \ddots & \vdots \\ A_{I(0)} & \cdots & A_{I(T)} \end{bmatrix} \quad (1)$$

Given the occurrence of an IE, the State Estimation module of the DBN-based AMST (yellow in Figure 1) estimates the probability that the NPP is running in the $\boldsymbol{z}$-th PDS by processing condition-monitoring data (i.e., $\boldsymbol{y}_{(0:k)}, \boldsymbol{\varphi}$):

$$p\left(\boldsymbol{Z}_{(k)} = \boldsymbol{z} \middle| \boldsymbol{y}_{(0:k)}, \boldsymbol{\varphi}, \boldsymbol{E}_{SE}\right) \quad (2)$$

where $\boldsymbol{E}_{SE}$ is the vector of the state estimation module parameters affected by epistemic uncertainty stemming either from the (weak) background modelling knowledge or the (non) comprehensiveness of scenarios used to make the inference. This uncertainty impacts on *i)* the selection of the variables deemed relevant for the analysis that form the $P_{tot} = p + q + (r + s + I)(T + 1)$ nodes of the DBN (i.e.,

$\boldsymbol{\phi}, \boldsymbol{Y}, \boldsymbol{\Psi}, \boldsymbol{X}, \boldsymbol{A}$) [21,22]; *ii)* the identification of the causal interdependence between the nodes (i.e., the DBN edges) [23–26]; iii) the definition of the CPTs parameters values [27–29]; and *iv)* the discretization of the continuous (i.e., non-discrete) nodes [30–32].

The risk predictor module of the DBN-based AMST (red in Figure 1), for each of the N_a alternative candidate sequences of mitigative actions (i.e., $\boldsymbol{A}_{(k+1:T)} = \boldsymbol{a}^{(j)}_{(k+1:T)}$, with $j = 1, \dots, N_a$), predicts at each future time step (i.e., $\forall\, i > k$) the ξ^{th} user-defined risk index, defined as the probability of leading the system into the ξ^{th} severe PDS $\boldsymbol{z}_\xi$ ($\xi = 1, \dots, \Xi$) (i.e., a subset of the system state space), conditioned on the j^{th} action undertaken:

$$R^{(j)}_{\xi(i)} = p\left(\boldsymbol{Z}_{(i)} = \boldsymbol{z}_\xi \middle| \boldsymbol{y}_{(0:k)}, \boldsymbol{\varphi}, \boldsymbol{a}^{(j)}_{(k+1:T)}, \boldsymbol{E}_{RP}\right), \text{ with } \xi = 1, \dots, \Xi,\ \forall\, i > k, \text{ and } j = 1, \dots, N_a \tag{3}$$

where $\boldsymbol{E}_{RP}$ is the vector of risk predictor module parameters affected by epistemic uncertainty (likewise $\boldsymbol{E}_{SE}$).

The uncertainty of $\boldsymbol{E}_{SE}$ and $\boldsymbol{E}_{RP}$ propagates to $R^{(j)}_{\xi(i)}$, whose uncertainty is called *residual uncertainty* and described by the probability distribution $p\left(R^{(j)}_{\xi(i)}\right)$.

In this work, we show that the proposed DBN-based AMST can quantify such residual uncertainty in terms of tolerance interval $\left[R^{(j)-}_{\xi(i)}, R^{(j)+}_{\xi(i)}\right]^{\beta}_{\gamma}$, where $R^{(j)-}_{\xi(i)}$ and $R^{(j)+}_{\xi(i)}$ are such that $\Pr\left(\int_{R^{(j)-}_{\xi(i)}}^{R^{(j)+}_{\xi(i)}} p\left(R^{(j)}_{\xi(i)}\right) dR^{(j)}_{\xi(i)} > \gamma\right) = \beta$, so to allow for a trustworthy decision on whether the j^{th} action is effective or not. Intuitively, the more comprehensive the scenarios used to learn the DBN CPTs parameters (with respect to the actual developing scenario and action being assessed), the lower the residual uncertainty (i.e., the narrower $\left[R^{(j)-}_{\xi(i)}, R^{(j)+}_{\xi(i)}\right]^{\beta}_{\gamma}$) and, thus, the more trustworthy the outcome $R^{(j)}_{\xi(i)}$.

2.1 Trustworthiness assessment

Let us consider a dataset of simulated severe accident scenarios $\boldsymbol{\mathcal{D}}$ and a DBN whose structure is fixed: for each n^{th} generic node $Z_{n=1,\dots,P_{tot}} \in \{\boldsymbol{\phi}, \boldsymbol{Y}, \boldsymbol{\Psi}, \boldsymbol{X}, \boldsymbol{A}\}$, the CPT is a Table of the form $\theta_{nmu} = \Pr(Z_n = u | Pa(Z_n) = m)$, for $u = 1, \dots, c_n$ and $m = 1, \dots, d_n$, where c_n is the number of values the node Z_n can take, $d_n = \prod_{v \in Pa(Z_n)} c_v$ is the number of combinations of the parents of Z_n (i.e., $Pa(Z_n)$), and $\sum_u \theta_{nmu} = 1$. If we assume that the likelihood of the data in $\boldsymbol{\mathcal{D}}$ is a multinominal distribution, the MLE of θ_{nmu} is [28]:

$$\hat{\theta}^{MLE}_{nmu} = \frac{N_{nmu}}{N_{nm}} \tag{4}$$

where $N_{nm1}, \dots, N_{nmc_n}$ are the number of times the events $(Z_n = 1|Pa(Z_n) = m), \dots, (Z_n = c_n|Pa(Z_n) = m)$ are observed in $\boldsymbol{\mathcal{D}}$, respectively, and $N_{nm} = \sum_u N_{nmu}$.

Intuitively, if $N_{nm} \approx 0$ (i.e., data in $\boldsymbol{\mathcal{D}}$ are not sufficient to cover some combinations of parent nodes states m), the MLE method is not accurate and the uncertainty about $\hat{\theta}_{nmu}^{MLE}$ increases because of the epistemic uncertainty stemming from the (non) comprehensiveness of $\boldsymbol{\mathcal{D}}$ [33], ultimately affecting the entire set of CPTs and the output of the risk predictor module.

To assess whether $\boldsymbol{\mathcal{D}}$ is comprehensive enough for trustworthy claiming that $\boldsymbol{a}_{(k+1:T)}^{(j)}$ is effective (or not) in mitigating the actual developing scenario, the trustworthiness assessment module (light green in Figure 1) uses a systematic approach based on Bayesian inference and the Monte Carlo (MC) method (see Appendix A) to duly account for the uncertainty of the CPTs parameters and propagate it to quantify the residual uncertainty of $R_{\xi(i)}^{(j)}$ $\left[R_{\xi(i)}^{(j)-}, R_{\xi(i)}^{(j)+}\right]_{\gamma}^{\beta}$; then, for each j^{th} sequence of candidate mitigative action $\boldsymbol{a}_{(k+1:T)}^{(j)}$, it determines whether this is *effective, non-effective* or *uncertain,* with trustworthiness:

- Effective with trustworthiness $\Leftrightarrow \left(\max_{i>k} R_{\xi(i)}^{(j)+}\right) < \epsilon_{\xi}$, for each risk index $\xi = 1,2, \dots, \Xi$;
- Non-effective with trustworthiness $\Leftrightarrow \left(\max_{i>k} R_{\xi(i)}^{(j)-}\right) > \epsilon_{\xi}$, for at least one risk index $\xi \in [1,2, \dots, \Xi]$;
- Non-trustworthy, otherwise.

where ϵ_{ξ} is a threshold set by the decision-maker for the ξ^{th} risk index. Figure 2 shows an illustrative example of effectiveness assessment carried out with respect to two risk indices (i.e., $\Xi = 2$): effectiveness with trustworthiness (Figure 2a), non-effectiveness with trustworthiness (Figure 2b and Figure 2c), non-trustworthiness for all the other cases (Figure 2d, Figure 2e and Figure 2f).

For defining the tolerance intervals, we take $\gamma = 0.90$ and $\beta = 0.95$ in line with NUREG-1855 [34] indication that the 5th and 95th percentiles (i.e., $\gamma = 0.90$) of any estimated risk index are suitable for characterizing uncertainty. Obviously, larger values for γ and β could be chosen if computational resources allow it, i.e., if the interval $\left[R_{\xi(i)}^{(j)-}, R_{\xi(i)}^{(j)+}\right]_{\gamma}^{\beta}$ can be computed for each $i > k$ quickly enough to support timely accident management (See Appendix A for the impact of γ and β on the computational burden).

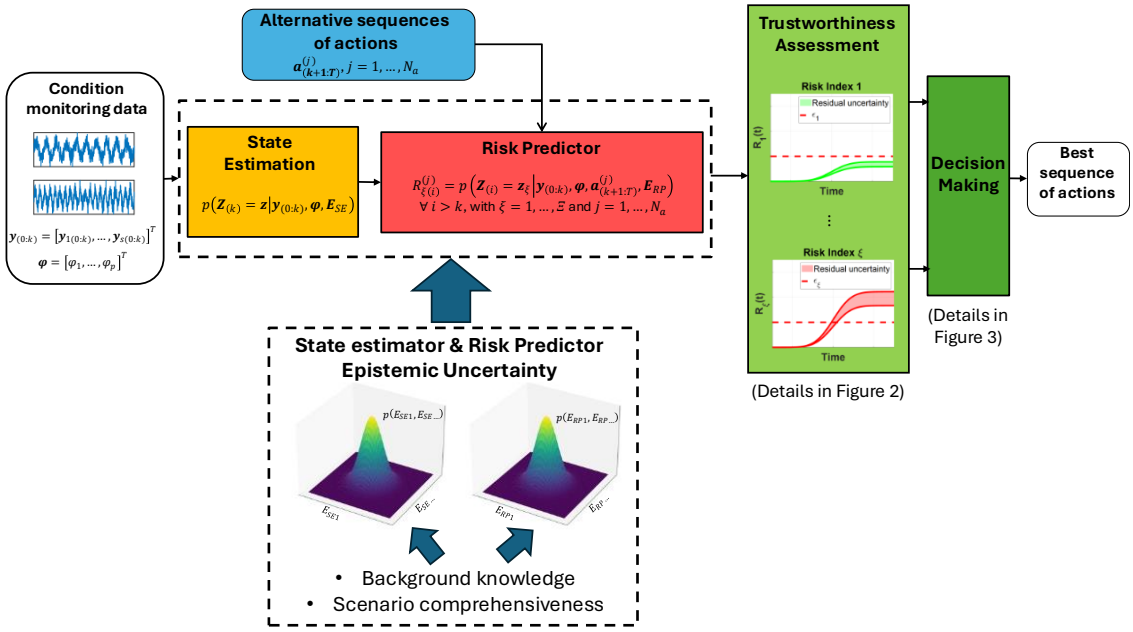

Figure 1. The AMST flowchart.

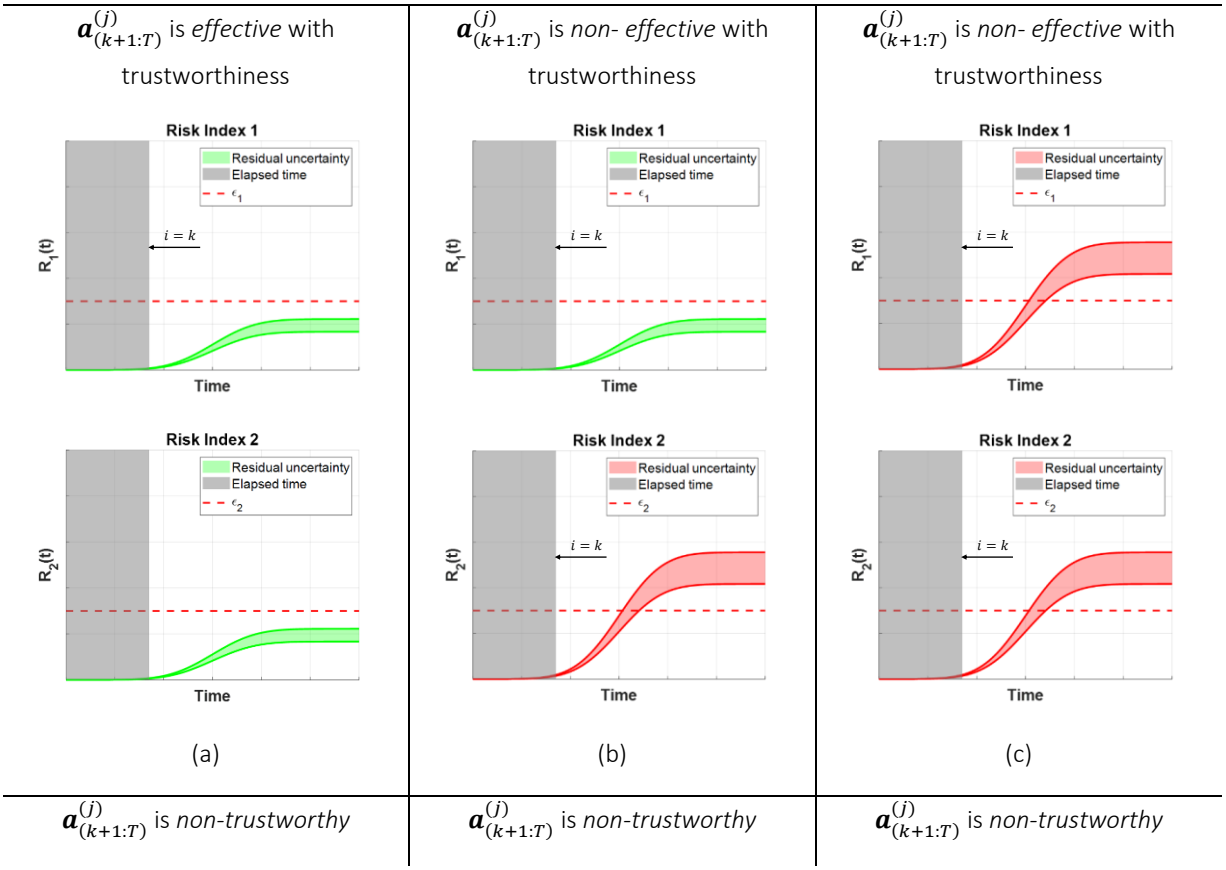

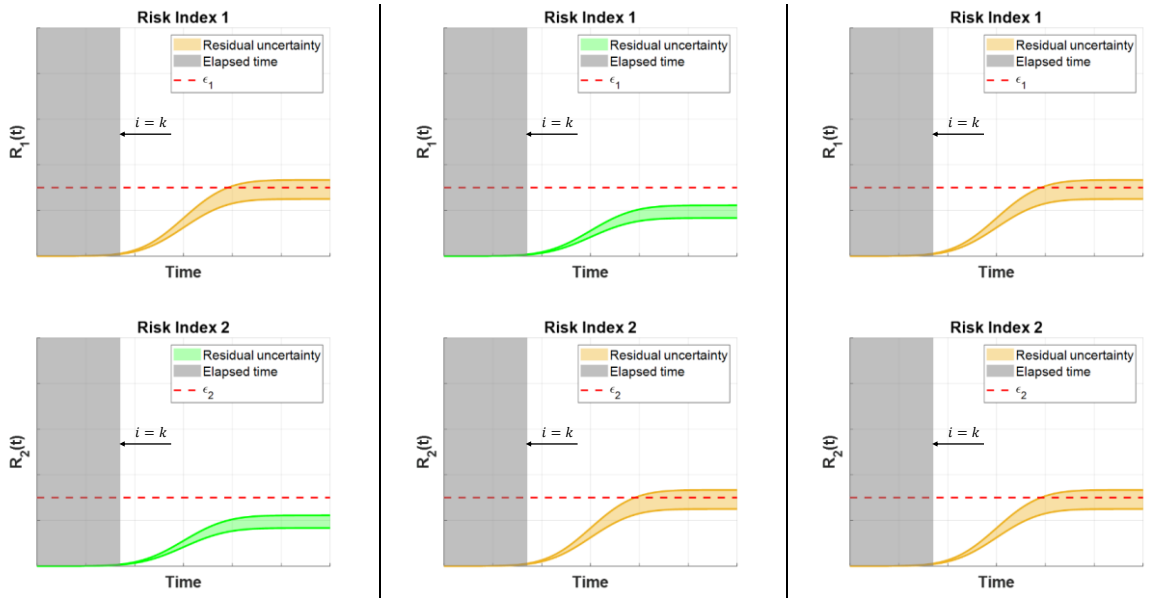

Figure 2. Some examples of effective, non- effective and non-trustworthy sequences of actions $\boldsymbol{a}^{(j)}_{(k+1:T)}$.

2.2 Multi-criteria decision-making under uncertainty

The decision on the selection of the best SAM strategy must consider not only the trustworthy effectiveness of the sequences of mitigative actions $\left\{\boldsymbol{a}^{(j)}_{(k+1:T)} | j = 1, \dots, N_a\right\}$ resulting as outcomes of the AMST, but also other criteria such as *feasibility* and *compatibility* with existing SAMGs. To address this, we employ a fuzzy set theory-based decision-making method of literature [17], which has been selected because it can handle vague, imprecise and uncertain information.

The multi criteria decision problem is here modelled by the hierarchical structure of Figure 3: the decision goal (Level 0) is the selection of the best severe accident management strategy (i.e., sequence of mitigative actions), and the evaluation criteria $\boldsymbol{C} = \{C_\lambda | \lambda = 1, \dots, \Lambda\}$ (Level 1) are *feasibility*, *effectiveness* and *compatibility* with existing SAMGs.

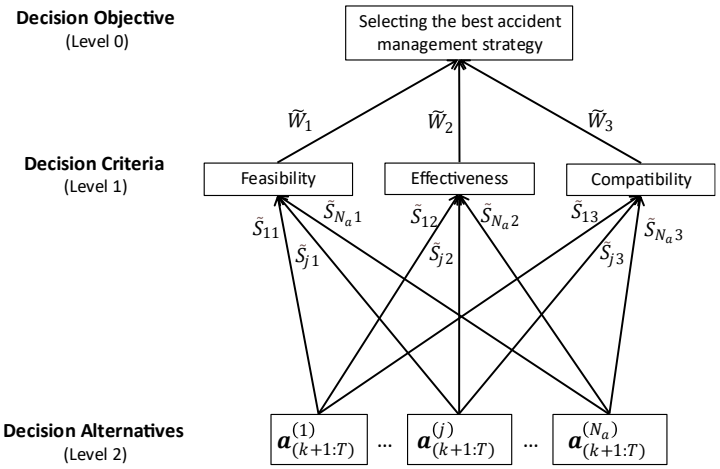

Figure 3. Hierarchical structure of the decision problem.

At level 2 each alternative action $\boldsymbol{a}_{(k+1:T)}^{(j)}$ is evaluated with respect to each criterion C_λ, whereas at Level 1 the importance of C_λ is evaluated with respect to the decision objective, with uncertainty represented by triangular fuzzy numbers (TFNs) $\tilde{S}_{j\lambda} = \left(d_{\tilde{S}_{j\lambda}}, e_{\tilde{S}_{j\lambda}}, f_{\tilde{S}_{j\lambda}}\right)$ and $\widetilde{W}_\lambda = \left(d_{\widetilde{W}_\lambda}, e_{\widetilde{W}_\lambda}, f_{\widetilde{W}_\lambda}\right)$, respectively (Figure 3). Each TFN is represented by a membership function defined by triplets $\left(d_{(\cdot)}, e_{(\cdot)}, f_{(\cdot)}\right)$, where $d_{(\cdot)} < e_{(\cdot)} < f_{(\cdot)}$, as:

$$\mu_{(\cdot)}(x) = \begin{cases} \dfrac{(x - d_{(\cdot)})}{(e_{(\cdot)} - d_{(\cdot)})} & d_{(\cdot)} \le x \le e_{(\cdot)} \\ \dfrac{(f_{(\cdot)} - x)}{(f_{(\cdot)} - e_{(\cdot)})} & e_{(\cdot)} \le x \le f_{(\cdot)} \\ 0 & otherwise \end{cases} \tag{5}$$

The TFNs $\tilde{S}_{j1} = \left(d_{\tilde{S}_{j1}}, e_{\tilde{S}_{j1}}, f_{\tilde{S}_{j1}}\right)$, $\tilde{S}_{j2} = \left(d_{\tilde{S}_{j2}}, e_{\tilde{S}_{j2}}, f_{\tilde{S}_{j2}}\right)$ and $\tilde{S}_{j3} = \left(d_{\tilde{S}_{j3}}, e_{\tilde{S}_{j3}}, f_{\tilde{S}_{j3}}\right)$ evaluate the *feasibility*, *effectiveness* and *compatibility* of $\boldsymbol{a}_{(k+1:T)}^{(j)}$, respectively, by mapping the opinion of the experts of the Technical Support Center (TSC) (i.e., the team that provides expert technical analysis, assessment, and makes decisions during severe accidents [1]) through a linguistic variable (i.e., "very low", "low", "medium", "high", "very high") into a TFN (Table 1 [17]) [35]. For example, if the experts believe that the *feasibility* of $\boldsymbol{a}_{(k+1:T)}^{(j)}$ is *very low* and the *compatibility medium* for the occurring scenario, $\tilde{S}_{j1} = (0, 0, 0.25)$ and $\tilde{S}_{j3} = (0.25, 0.5, 0.75)$.

In the methodological framework here proposed, the *effectiveness* of $\boldsymbol{a}_{(k+1:T)}^{(j)}$ (i.e., the capability of a sequence of actions to prevent the system from entering a severe PDS) is evaluated by considering the

lower and upper bounds of the uncertainty associated with the risk index $R_{\xi(i)}^{(j)}$, namely $R_{\xi(i)}^{(j)-}$ and $R_{\xi(i)}^{(j)+}$ (see Section 2.1), and $R_{\xi(i)}^{(j)MLE}$, that is the risk index computed using the MLE of the CPTs $\hat{\theta}_{nmu}^{MLE}$.

Specifically, the lower, central and upper values of $\tilde{S}_{j2}$ (Eq. 6) are computed as $\min_{i>k}\left(1-R_{(i)}^{(j)+}\right)$, $\min_{i>k}\left(1-R_{(i)}^{(j)MLE}\right)$ and $\min_{i>k}\left(1-R_{(i)}^{(j)-}\right)$, respectively; where $\min_{i>k}\left(1-R_{(i)}^{(j)\cdot}\right)$ is the minimum (i.e., most conservative) probability that the system will not enter a severe PDS, given the implementation of $\boldsymbol{a}_{(k+1:T)}^{(j)}$, for all $i > k$:

$$\tilde{S}_{j2} = \left(\min_{i>k}\left(1-R_{(i)}^{(j)+}\right), \min_{i>k}\left(1-R_{(i)}^{(j)MLE}\right), \min_{i>k}\left(1-R_{(i)}^{(j)-}\right)\right) \tag{6}$$

If more than one risk index is considered in the analysis (i.e., $\Xi > 1$), the effectiveness is assessed for each ξ^{th} severe PDS ($\xi = 1,2,\dots,\Xi$) through $\tilde{S}_{j\xi 2} = \left(\min_{i>k}\left(1-R_{\xi(i)}^{(j)-}\right), \min_{i>k}\left(1-R_{\xi(i)}^{(j)MLE}\right), \min_{i>k}\left(1-R_{\xi(i)}^{(j)-}\right)\right)$ and, then, averaged according to TFNs importance weights $\widetilde{W}_{\xi} = \left(d_{\widetilde{W}_{\xi}}, e_{\widetilde{W}_{\xi}}, f_{\widetilde{W}_{\xi}}\right)$, which can be assigned by decision makers to each ξ^{th} severe PDS, again, through linguistic variables (i.e., “very low”, ”low”, ”medium”, ”high”, “very high”), then converted into TFNs (Table 1):

$$\tilde{S}_{j2} = \left(\frac{1}{\Xi}\sum_{\xi=1}^{\Xi} d_{\widetilde{W}_{\xi}} d_{\tilde{S}_{j\xi 2}}, \frac{1}{\Xi}\sum_{\xi=1}^{\Xi} e_{\widetilde{W}_{\xi}} e_{\tilde{S}_{j\xi 2}}, \frac{1}{\Xi}\sum_{\xi=1}^{\Xi} f_{\widetilde{W}_{\xi}} f_{\tilde{S}_{j\xi 2}}\right) \tag{7}$$

At Level 1, the importance weights $\widetilde{W}_{\lambda} = \left(d_{\widetilde{W}_{\lambda}}, e_{\widetilde{W}_{\lambda}}, f_{\widetilde{W}_{\lambda}}\right)$ of the criteria are also determined by expert judgement in terms of linguistic variables (i.e., “very low”, ”low”, ”medium”, ”high”, “very high” level), with the corresponding TFNs of Table 1.

Finally, for each alternative $\boldsymbol{a}_{(k+1:T)}^{(j)}$ the overall fuzzy score $\tilde{F}_j = (d_{\tilde{F}_j}, e_{\tilde{F}_j}, f_{\tilde{F}_j})$ with respect to the decision objective is computed as the fuzzy weighed sum of all the criteria:

$$\tilde{F}_j = \left(\frac{1}{\Lambda}\sum_{\lambda=1}^{\Lambda} d_{\widetilde{W}_{\lambda}} d_{\tilde{S}_{j\lambda}}, \frac{1}{\Lambda}\sum_{\lambda=1}^{\Lambda} e_{\widetilde{W}_{\lambda}} e_{\tilde{S}_{j\lambda}}, \frac{1}{\Lambda}\sum_{\lambda=1}^{\Lambda} f_{\widetilde{W}_{\lambda}} f_{\tilde{S}_{j\lambda}}\right) \tag{8}$$

and $\left\{\boldsymbol{a}_{(k+1:T)}^{(j)} | j = 1,\dots,N_a\right\}$ are ranked based on the computed triangular fuzzy numbers $\{\tilde{F}_j | j = 1,\dots,N_a\}$. Various approaches for ranking fuzzy numbers have been proposed in the literature [36–38]. In this study, the total integral value method is employed due to its ease of application. The total integral value for a triangular fuzzy number $F = (d, e, f)$ is defined as [38]:

$$I_T^{\delta} = \frac{1}{2}[(1-\delta)d + e + \delta f] \tag{9}$$

where $0 \le \delta \le 1$ is an index commonly referred to in the literature as *index of optimism* or *degree of optimism* [37]. For example, if decision makers want to be conservative and, thus, rely more on a pessimistic (i.e., close to the lower bound d) estimate of I_T^{δ}, δ is set equal to $\delta = 0$, resulting in $d < I_T^{\delta=0} < e$.

Conversely, $\delta = 1$ means that the decision makers are more optimistic and, thus, values closer to the upper bound f are considered. The value of $\delta = 0.5$ is customarily adopted for decision-making in the context of severe accident management [35], because this allows decision-makers to be neither too pessimistic nor too optimistic.

Given two fuzzy numbers F_i and F_j, the ranking is determined as follows: if $I_T^{\delta}(F_i) < I_T^{\delta}(F_j)$, then $F_i < F_j$; if $I_T^{\delta}(F_i) = I_T^{\delta}(F_j)$, then $F_i = F_j$; and if $I_T^{\delta}(F_i) > I_T^{\delta}(F_j)$, then $F_i > F_j$. For a detailed description about the ranking of TFN through integral values and the informed selection of the *degree of optimism*, the reader can refer to [38]. In the methodological framework of SAM here of interest, the alternative $\boldsymbol{a}_{(k+1:T)}^{(j)}$ with the highest total integral value is considered to be the best decision.

Table 1. Triangular fuzzy number corresponding to each linguistic variable and corresponding triangular fuzzy number.

Linguistic variable	Very low	Low	Medium	High	Very high
Fuzzy number	$(0, 0, 0.25)$	$(0, 0.25, 0.5)$	$(0.25, 0.5, 0.75)$	$(0.5, 0.75, 1)$	$(0.75, 1, 1)$

3 Case Study

The proposed methodological framework for SAM informed by AMST outcomes is exemplified with respect to the possible severe escalation of transients initiated by LOCAs (i.e., $\Psi_{IE} = LOCA$) in a WWER-1000/V446 NPP operating at full power (i.e., $\Psi_{POC} = full\ power$). Figure 4 sketches the considered NPP, whose technical specifications are provided in Table 2 [39]. In the event of a LOCA, the CB, whose relevant parameters are listed in Table 3, may suffer of inner pressure overload, either because of the steam released by the primary circuit or the explosion caused by the hydrogen. In LOCA circumstances, SAMGs advise either to initiate the Filtered Containment Venting (FCV) to prevent containment overpressure—accepting a limited release of fission products—or to delay venting to utilize the spray system for controlling containment pressure [2]. However, activating the spray system requires careful evaluation, as it induces steam condensation that increases hydrogen concentration within the containment, thereby increasing the probability of hydrogen combustion. The objective of the application is to show how to exploit the DBN-based AMST outcomes with trustworthiness for effective SAM decision-making. For comparison, the MLE-learned DBN AMST outcomes, that neglect the residual uncertainty in the risk indices, are also considered.

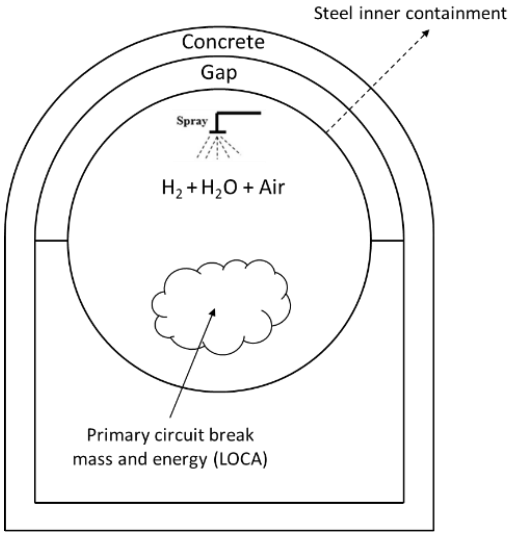

Figure 4. Schematic representation of the WWER-1000/V446 CB structure (specifications are given in Table 3).

Table 2. Specifications of the WWER-1000/V446 NPP [40].

Parameter	Value
Core nominal thermal power (Mw)	3000
Average coolant temperature at reactor outlet (K)	594
Maximum coolant temperature at reactor inlet (K)	564
Primary circuit pressure (MPa)	15.7
Pressure drop in the core (MPa)	0.381

Table 3. Relevant parameters of the WWER-1000/V446 containment [39,40].

Parameter	Value
Spray system flowrate (kg/s)	166.67
Steel containment inner radius (mm)	28000
Steel thickness (mm)	30
Gap thickness (mm)	1650
Concrete thickness (mm)	1750
Containment free volume (m^3)	71040
Maximum internal pressure at 150 °C (MPa)	0.46

Total area of all the concrete walls (m^2)	18860
Total surface area of the steel containment (m^2)	17712

To generate the accident scenarios, the TH model of the primary circuit and the CB model have been coupled with a hydrogen combustion model to simulate the accident over a transient period of $T_m = 3600\,s$ and provide the output data (i.e., $\dot{m}_{BR}(t)$, $p_{cont}(t)$, $T_{cont}(t)$, $X_{H2O}(t)$, $X_{H2}(t)$, $C_{regime}(t)$, described below) every $\Delta t = 100\,s$ (i.e., emulating a condition-monitoring frequency of $0.01\,Hz$) (Figure 5).

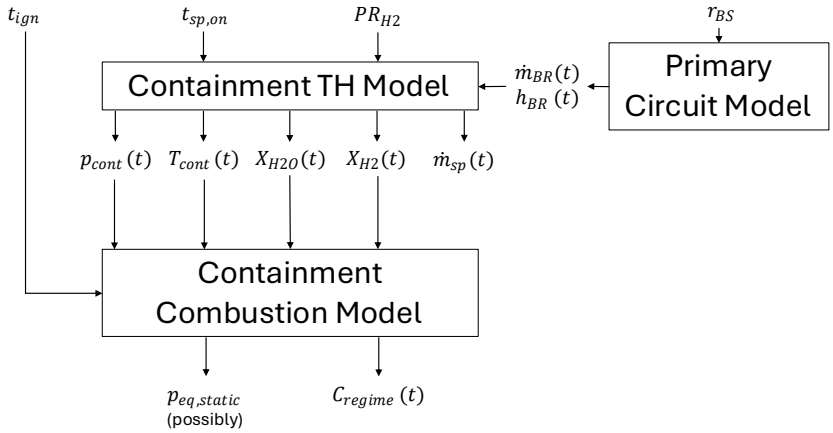

Figure 5. Structure of the physical model of the system.

A detailed description of the models governing equations, implemented in a MATLAB/Simulink® routine, are provided in Appendix B. In summary, the water flowrate $\dot{m}_{BR}(t)$ released into the containment during the LOCA is computed adopting a homogeneous equilibrium model [41], where the RCS primary circuit is modeled as an ideal pressurized vessel with a bottom break radius r_{BS}. The containment TH model takes as inputs $\dot{m}_{BR}(t)$, the hydrogen production rate PR_{H2} (i.e., the mass of hydrogen released into the containment per unit time, net of the amount absorbed by passive autocatalytic recombiners (PARs)), the ignition time t_{ign} and the spray system activation time $t_{sp,on}$, and predicts the containment time-dependent pressure $p_{cont}(t)$, the temperature $T_{cont}(t)$, the steam molar fraction $X_{H2O}(t)$ and the hydrogen molar fraction $X_{H2}(t)$ within the CB, along with the spray system flowrate $\dot{m}_{sp}(t)$. The spray system activates only if $p_{cont}(t) > 1.3\,Bar$ and stops when $p_{cont}(t) < 0.98\,Bar$. The containment combustion model, developed following [42,43], takes $p_{cont}(t)$, $T_{cont}(t)$, $X_{H2O}(t)$ and $X_{H2}(t)$, and assesses at any time t the hydrogen combustion regime $C_{regime}(t)$ that would result from an hypothetical ignition at that time:

$$C_{regime}(t) = \begin{cases} 0 & \text{if the CB hydrogen} - \text{air mixture is nonflammable at } t \\ 1 & \text{if the CB hydrogen} - \text{air mixture is flammable at } t \\ 2 & \text{if ignition at } t \text{ leads to Flame Acceleration} \\ 3 & \text{if ignition at } t \text{ leads to Deflagration} - \text{to} - \text{Detonation Transition} \\ 4 & \text{if ignition at } t \text{ leads to Detonation} \end{cases} \quad (10)$$

If $C_{regime}(t_{ign}) > 0$: i) the Simulink simulation stops; ii) the static pressure load on the CB resulting from hydrogen combustion $p_{eq,static}$ is computed [44]; iii) the CB hydrogen-air mixture conditions right after the combustion (i.e., $p_{cont}(t_{ign} + \Delta t)$, $T_{cont}(t_{ign} + \Delta t)$, $X_{H2O}(t_{ign} + \Delta t)$ and $X_{H2}(t_{ign} + \Delta t)$) are calculated and set as initial conditions for the Simulink TH model that completes the simulation between $t_{ign} + \Delta t$ and T_m. For example, in Figure 6 we show $p_{cont}(t)$ and $C_{regime}(t)$ for a simulation with $r_{BS} = 0.05\ m$, $PR_{H2} = 0.25\ kg/s$, $t_{sp,on} = 800\ s$ and $t_{ign} = 3000\ s$: we can notice that the derivative of $p_{cont}(t)$ changes at the activation of the spray system and at the time in which $\dot{m}_{BR}(t) = 0$; moreover, the CB hydrogen-air mixture is flammable from $t = 2500\ s$ (i.e., $C_{regime}(t) > 0$), and after the combustion returns to nonflammable (i.e., $C_{regime}(t) = 0$) because all the hydrogen is burnt.

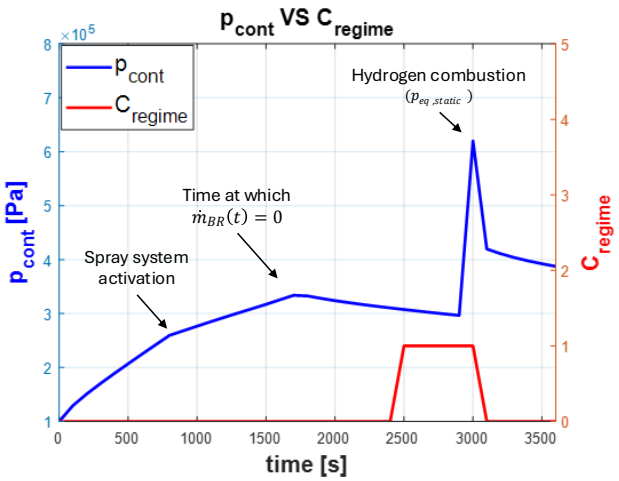

Figure 6. Comparison between $p_{cont}(t)$ and $C_{regime}(t)$ for a transient characterized by $r_{BS} = 0.05m$, $PR_{H2} = 0.25\ kg/s$, $t_{sp,on} = 800\ s$ and $t_{ign} = 3000\ s$.

The DBN that models these phenomena is built with GeNIe [45], and its application is carried out in SMILE v.2.0.10, where the Estimated Posterior Importance Sampling (EPIS) algorithm [46] is adopted to infer Eqs. (2-3).

Figure 7 shows the DBN, consisting of $T + 1$ unrolled time slices (only two consecutive time slices are shown in Figure 7), whose nodes and interdependencies have already been described in [11] and here only briefly summarized below:

- Ψ_{POC}: static hidden node representing the initial plant operating conditions, reasonably impacting the IE (i.e., Ψ_{IE}), and the primary circuit initial pressure and temperature (i.e., ϕ_{pP0} and ϕ_{pT0}, respectively). For this case study, we assumed $\Psi_{POC} = full\ power$.
- Ψ_{IE}: static hidden node indicating the IE, reasonably affecting the break size and the hydrogen production rate (i.e., $\Psi_{r_{BS}}$ and $\Psi_{PR_{H_2}}$). In this case study, we set $\Psi_{IE} = LOCA$.
- ϕ_{pP0}: static observable node representing the primary circuit initial pressure. It influences the containment pressure $Y_{p_{cont(k)}}$ and temperature $Y_{T_{cont(k)}}$. In this case study, $\phi_{pP0} = 15.7\ Mpa$.
- ϕ_{pT0}: static observable variable node representing the primary circuit initial temperature. It influences $Y_{p_{cont(k)}}$ and $Y_{T_{cont(k)}}$. In this case study, $\phi_{pT0} = 579\ K$.
- $\Psi_{r_{BS}}$: static hidden node of the break size on the primary circuity, which affects the containment pressure $Y_{p_{cont(k)}}$ and temperature $Y_{T_{cont(k)}}$, and the molar fractions of the steam $Y_{X_{H2O_{(k)}}}$ and hydrogen $Y_{X_{H2_{(k)}}}$.
- $\Psi_{PR_{H_2}}$: static hidden node of the hydrogen production rate, which affects $Y_{p_{cont(k)}}$, $Y_{T_{cont(k)}}$, $Y_{X_{H2O_{(k)}}}$ and $Y_{X_{H2_{(k)}}}$;
- $X_{C_{reg}(k)}$: dynamic hidden node influenced by $Y_{X_{H2O_{(k)}}}$, $Y_{X_{H2_{(k)}}}$, $Y_{p_{cont(k)}}$ and $Y_{T_{cont(k)}}$ (in line with the containment combustion model of Figure 5);
- $Y_{sp_{(k)}}$: observable dynamic node describing the real operational state of the spray system, defined as:

$$Y_{sp_{(k)}} = \begin{cases} 0 & if\ \dot{m}_{sp}(t_k) = 0 \\ 1 & if\ \dot{m}_{sp}(t_k) > 0 \end{cases} \tag{11}$$

  which depends on $Y_{p_{cont(k)}}$ and $A_{sp_{(k)}}$ (i.e., the action carried out by the operators on the spray system at time step k), which is defined as:

$$A_{sp_{(k)}} = \begin{cases} 1 & \text{if the spray system is activated at } k \\ 2 & \text{if the spray system is kept inactive at } k \\ 3 & \text{if the spray system is deactivated at } k \\ 4 & \text{if the spray system is kept active at } k \end{cases} \tag{12}$$

The CB is assumed damaged if $p_{cont}(t)$ exceeds the CB design pressure p_{des}. Thus, the CB damage state $X_{CB_{DS}(k)}$ is affected by $Y_{p_{cont(k)}}$, and defined as:

$$X_{CB_{DS}(k)} = \begin{cases} 1 & if\ T_{p_{cont}>p_{des}} \leq t_k \\ 0 & \text{otherwise} \end{cases} \tag{13}$$

where $T_{p_{cont}>p_{des}}$ is the time at which the $p_{cont}(t)$ exceeds the CB design pressure p_{des} (i.e., $X_{CB_{DS}(k)} = 1$, CB damaged, and $X_{CB_{DS}(k)} = 0$, CB safe). Thus, the (only) risk index considered in this case study is related to the probability that the CB is damaged by the internal load and is defined as:

$$R_{CB(i)}^{(j)} = p\left(X_{CB_{DS}(k)} = 1 | \boldsymbol{y}_{(0:k)}, \boldsymbol{a}_{sp(k+1:T)}^{(j)}\right), \forall\ i > k, \text{ and } j = 1, \dots, N_a \tag{14}$$

Regarding inter-slice dependencies, each dynamic node at time k is connected to its counterpart at time $k+1$, except for $Y_{sp_{(k)}}$, whose state is determined by $A_{sp_{(k)}}$ and $Y_{p_{cont(k)}}$. Additionally, it is assumed that the activation of the spray system at time k influences $p_{cont}(t)$ and $T_{cont}(t)$ at time step $k+1$; thus, two directed edges from $Y_{sp_{(k)}}$ towards $Y_{p_{cont(k+1)}}$ and $Y_{T_{cont(k+1)}}$ are incorporated into the DBN structure. Table 16 (in Appendix C) summarizes the DBN nodes characterization and their parent–child dependencies across static and dynamic variables.

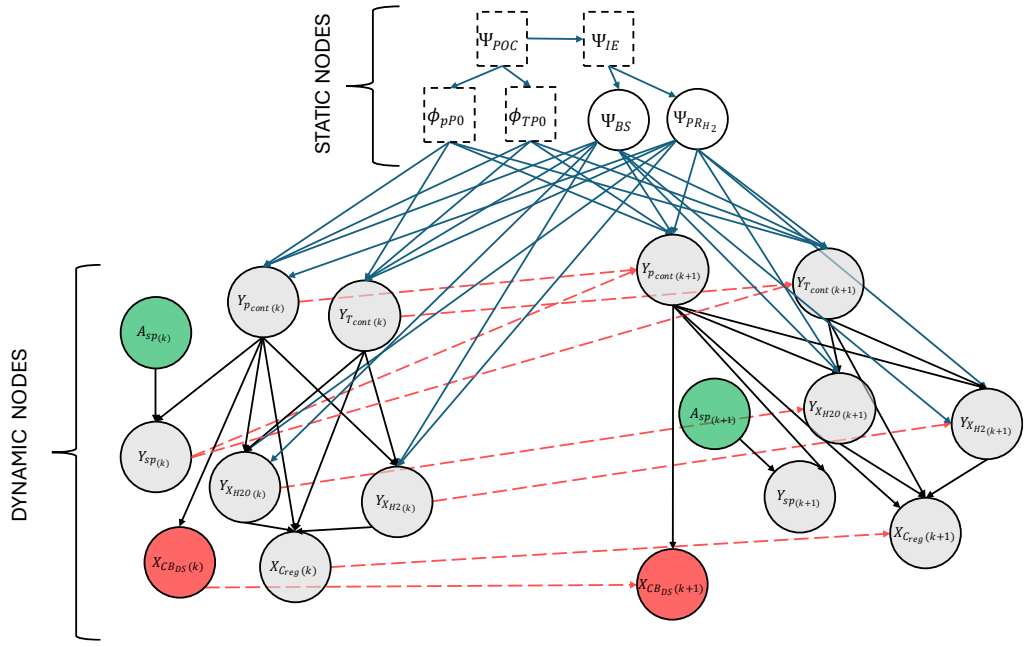

Figure 7. The proposed DBN structure unrolled over two consecutive time steps. Black edges indicate intra-slice dependencies, red-dotted edges denote inter-slice dependencies, and blue edges represent dependencies involving static variables. Green nodes indicate operator actions, red nodes the damage states of the safety barriers, gray nodes the generic dynamic variables, and white nodes the static variables.

The learning of the CPTs parameters values is based on $N_{CPT} = 6 \times 10^3$ stochastic scenarios generated by sampling the models input parameters from uniform probability distributions whose upper and lower bounds are listed in Table 4. The range of variation of the probability distribution of PR_{H2} is taken equal to $\pm 50\%$ of its nominal value (i.e., $0.2\ kg/s$ [47]) to reflect its significant epistemic uncertainty. The aleatory uncertainty that affects r_{BS} is described by the lower and upper bounds of its distribution, whose values are set equal to $0.006\ m$ (i.e., the lowest primary circuit boundary break radius assumed by the NRC for a Small LOCA [48]) and $0.212\ m$ (i.e., the lowest r_{BS} that would make $\dot{m}_{BR}(t) = 0$ within $\Delta t = 100\ s$: any larger

value would, therefore, not be "noticed" by the DBN), whereas $t_{sp,on}$ and t_{ign} can take any value between 0 and T_m.

Table 4. Upper and Lower bounds of the uniform probability distributions of the model input parameters.

Input parameter	Description	Nominal Value	Lower Bound	Upper Bound
$r_{BS}\ (m)$	Break size on the primary circuit	-	0.006 ([48])	0.212
$PR_{H2}\ \left(\frac{kg}{s}\right)$	Hydrogen production rate, net of that absorbed by PARs	0.2 ([47])	0.1	0.3
$t_{sp,on}\ (s)$	Spray system activation time	-	0	3600
$t_{ign}\ (s)$	Ignition time	-	0	3600

The $N_{CPT} \times P_{tot}$ data matrix $\boldsymbol{\mathcal{D}}$ populated with the generated scenarios is, then, used to infer the CPTs parameters and evaluate their uncertainty, as described in Appendix A.

We test the decision taken with the support of the DBN-based AMST for two scenarios: scenario 1 is a large LOCA with a nominal PR_{H2} (i.e., $r_{BS} = 0.2\ m$ and $PR_{H2} = 0.2\ kg/s$); scenario 2 is a small LOCA with a small PR_{H2} (i.e., $r_{BS} = 0.025\ m$ and $PR_{H2} = 0.1\ kg/s$). For each scenario, we analyze three alternative mitigative actions (i.e., $N_a = 3$): $\boldsymbol{a}^{(1)}_{sp(0:T)}$ consists in the activation of the spray system at $t_{sp,on} = 1500\ s$; $\boldsymbol{a}^{(2)}_{sp(0:T)}$ consists in the activation of the spray system at $t_{sp,on} = 2500\ s$; $\boldsymbol{a}^{(3)}_{sp(0:T)}$ consists in not activating the spray system (i.e., $t_{sp,on} = +\infty$). In both scenarios, the ignition time is set equal to $t_{ign} = 3500\ s$ and the evidence, represented by sensor data from the NPP (i.e., $y_{p_{cont}(0:k)}$, $y_{T_{cont}(0:k)}$, $y_{X_{H2}(0:k)}$, $y_{X_{H2O}(0:k)}$, $y_{sp(0:k)}$), is obtained using the physical model. None of the two considered scenarios is included in $\boldsymbol{\mathcal{D}}$.

For both scenarios, the effectiveness and trustworthiness of the three candidate mitigative actions are evaluated at $k = 10,20,30$; this is done by computing the non-parametric tolerance interval $\left[R^{(j)-}_{CB(i)}, R^{(j)+}_{CB(i)}\right]^{\beta}_{\gamma}$ for each $i > k$, and comparing them to the threshold ϵ_{CB} specified by the decision-maker.

The coverage γ and the confidence level β are set to $\gamma = 0.95$, $\beta = 0.95$ (resulting in $N^{\beta}_{\gamma} = 93$ [49]), allowing for a sufficiently fast computation (see Section 4), in compliance with the setting criteria discussed in Section 2.1. The risk threshold ϵ_{CB} is set equal to $\epsilon_{CB} = 0.05$ to preserve the conservative safety margin with respect to the CCFP $p_{CCF} = 0.1$ (that is recommended by the NRC [50]), needed to accommodate errors introduced by the discretized DBNs [51].

Without loss of generality, the hierarchical structure of Figure 3 is adopted to perform the decision-making among the alternatives $\boldsymbol{a}^{(1)}_{sp(0:T)}, \boldsymbol{a}^{(2)}_{sp(0:T)}, \boldsymbol{a}^{(3)}_{sp(0:T)}$, with decision criteria "*Feasibility*", "*Effectiveness*" and "*Compatibility*". The assumed linguistic variables and the corresponding TFNs (determined through Table 1) assigned to the importance weights of the decision criteria are listed in Table 5. Analogously, Table 6 lists the assumed linguistic variables and the corresponding TFNs assigned to the decision alternatives with

respect to *Feasibility* and *Compatibility*. The fuzzy *effectiveness* of the alternatives is computed following Eqs. (6-8).

Table 5. Linguistic variables (and corresponding TFNs) assigned to the criteria importance weights.

Criterion	Importance weight ($\widetilde{W}_\lambda$)
Feasibility	High $(0.5, 0.75, 1)$
Effectiveness	Very High $(0.75, 1, 1)$
Compatibility	High $(0.5, 0.75, 1)$

Table 6. Linguistic variables (and corresponding TFNs) assigned to the decision alternative with respect to Feasibility and Compatibility.

Alternatives	*Feasibility* ($\tilde{S}_{j1}$)	*Compatibility* ($\tilde{S}_{j3}$)
$\boldsymbol{a}_{sp(0:T)}^{(1)}$	Very High $(0.75, 1, 1)$	Very High $(0.75, 1, 1)$
$\boldsymbol{a}_{sp(0:T)}^{(2)}$	Very High $(0.75, 1, 1)$	Very High $(0.75, 1, 1)$
$\boldsymbol{a}_{sp(0:T)}^{(3)}$	Very High $(0.75, 1, 1)$	Very High $(0.75, 1, 1)$

4 Results

The computations have been performed using a dual-core processor with a clock speed of 2.7 GHz and 3.5 GHz in normal and TurboBoost modes. The Computational Times CT for $k = 10$, $k = 20$ and $k = 30$, are $CT = 20\,s$, $CT = 13\,s$ and $CT = 7\,s$, respectively, that allow, in all cases, for a timely accident management, being the Δt between two successive sensors data acquisition and the resulting DBN inferences equal to $100\,s$.

4.1 Scenario 1: large LOCA with a nominal hydrogen production rate

Figure 8, Figure 9 and Figure 10 show the risk index residual uncertainty computed at $k = 10, 20, 30$, respectively and used for determining the trustworthy effectiveness of the candidate mitigative actions. Specifically, each sub-plot shows: i) the lower bound $R_{CB(i)}^{(j)-}$ (green line) and upper bound $R_{CB(i)}^{(j)+}$ (red line) of the risk index residual uncertainty for each $i > k$, corresponding to the j^{th} action analyzed, $\boldsymbol{a}_{sp_{(0:T)}}^{(j)}$; ii) the inference results obtained via a MLE-learned DBN $R_{CB(i)}^{MLE(j)}$ (i.e., without uncertainty propagation) for

comparison (blue line); iii) the ground truth $R_{CB(i)}^{GT(j)}$ (i.e., the actual value of $R_{CB(i)}^{(j)}$, simulated through the physical model) (black line).

Examining $R_{CB(i)}^{GT(j)}$, we note that activating the spray system either too early (i.e., $\boldsymbol{a}_{(0:T)}^{(1)}$) or too late (i.e., $\boldsymbol{a}_{(0:T)}^{(3)}$) leads to the system failure at $i = 35$ and $i = 27$, respectively (i.e., $R_{CB(i)}^{GT(1)} = 1$ for $i \geq 35$ and $R_{CB(i)}^{GT(3)} = 1$ for $i \geq 27$); conversely, $\boldsymbol{a}_{(0:T)}^{(2)}$ successfully mitigates the accident (i.e., $R_{CB(i)}^{GT(2)} = 0\ \forall i$). Indeed, an excessively early activation of the spray system limits the increase in pressure and temperature within the CB, but it also induces steam condensation, potentially increasing hydrogen concentrations and thereby increasing the probability of hydrogen combustion. On the other hand, excessively delayed activation or the absence of spray system activation fails to prevent the CB pressure from reaching its design limit due to steam release from the LOCA.

We also observe that: i) we should not trust $\boldsymbol{a}_{(0:T)}^{(1)}$ since neither $\left(\max_{i>k} R_{CB(i)}^{(1)+}\right) < \epsilon_{CB}$ nor $\left(\max_{i>k} R_{CB(i)}^{(1)-}\right) > \epsilon_{CB}$) hold, making its effectiveness uncertain; ii) $\boldsymbol{a}_{(0:T)}^{(2)}$ is effective and trustworthy (i.e., $\left(\max_{i>k} R_{CB(i)}^{(2)+}\right) < \epsilon_{CB}$); iii) $\boldsymbol{a}_{(0:T)}^{(3)}$ is non-effective and trustworthy (i.e., $\left(\max_{i>k} R_{CB(i)}^{(3)-}\right) > \epsilon_{CB}$). From this perspective, the proposed methodology offers a criterion to determine whether $\boldsymbol{a}_{(k+1:T)}^{(j)}$ is effective or not for the specific developing scenario. In this specific case, $\boldsymbol{\mathcal{D}}$ is not enough comprehensive to assess whether $\boldsymbol{a}_{(0:T)}^{(1)}$ is effective for scenario 1.

Table 7, Table 8 and Table 9 show the results of the decision-making process carried out at $k = 10, 20, 30$, respectively. Specifically, each Table reports, for the alternatives $\boldsymbol{a}_{sp_{(0:T)}}^{(1)}$ and $\boldsymbol{a}_{sp_{(0:T)}}^{(2)}$: i) their fuzzy *Effectiveness* $\tilde{S}_{j2}$, ii) their overall fuzzy score $\tilde{F}_j$ and iii) their total integral value $I_T^{\delta}(\tilde{F}_j)$ computed at $\delta = 0.0, 0.5, 1.0$ to represent the choice of the decision maker to rely on the lower bound, modal and upper bound values of $\tilde{F}_j$ for decision-making (pessimistic, moderate or optimistic, respectively) [17]. Results for $\boldsymbol{a}_{sp_{(0:T)}}^{(3)}$ are not reported, as it is trustworthy non-effective. Since no distinction is made for the alternatives in terms of *Feasibility* and *Compatibility* (see Table 6), the ranking of the best alternative in this case study is solely determined by the *Effectiveness*. Consequently, $\boldsymbol{a}_{sp_{(0:T)}}^{(2)}$ is ranked as the best alternative, as it is the only *effective* and trustworthy sequence of actions, $\boldsymbol{a}_{sp_{(0:T)}}^{(1)}$ is uncertain, and $\boldsymbol{a}_{sp_{(0:T)}}^{(3)}$ is *non-effective* (i.e., $\left(\max_{i>k} R_{CB(i)}^{(3)-}\right) > \epsilon_{CB}$). The results, therefore, are found to align well with the ground truth.

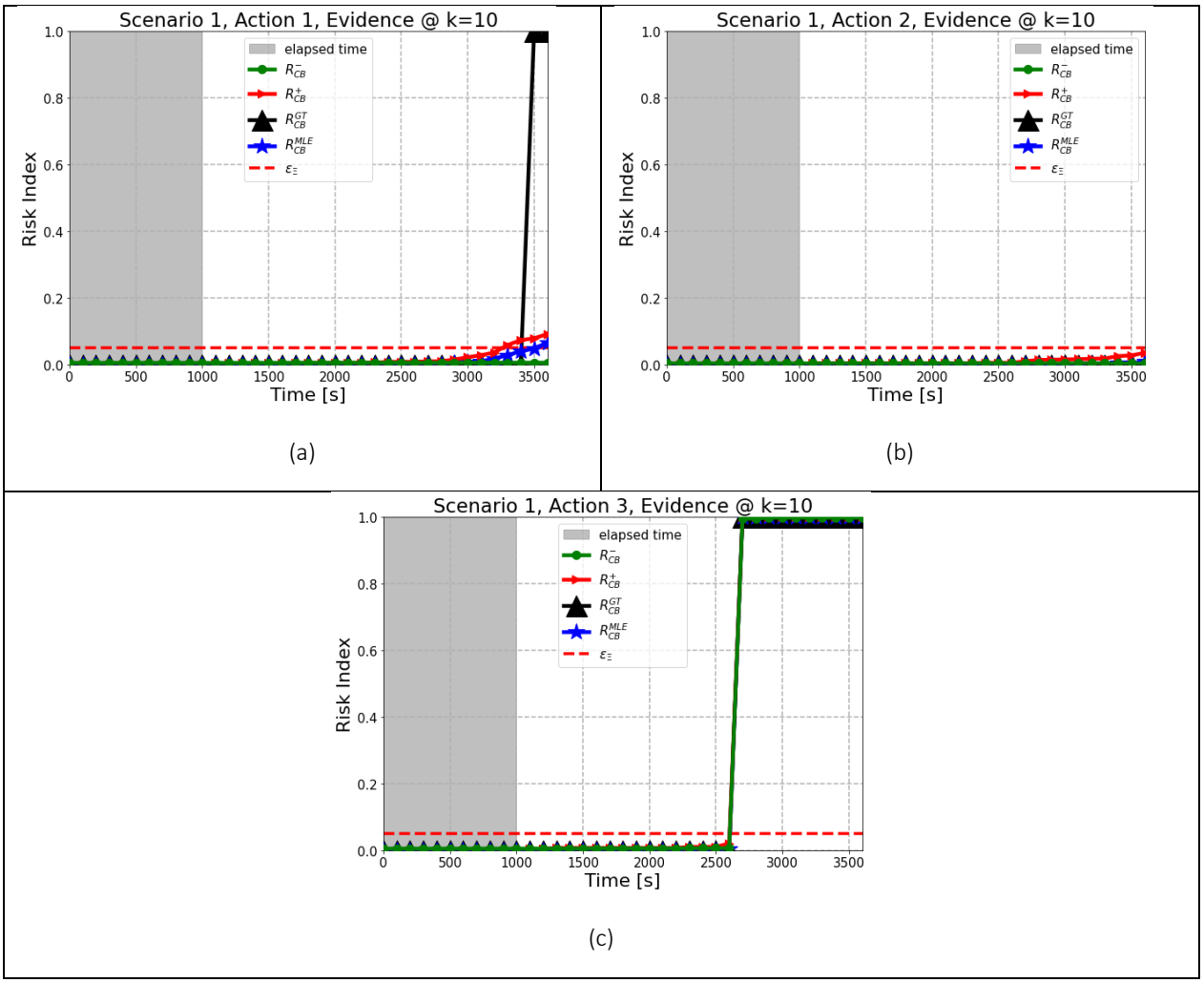

Figure 8. Lower bound $\boldsymbol{R}_{\boldsymbol{CB(i)}}^{\boldsymbol{(j)-}}$ (green line) and upper bound $\boldsymbol{R}_{\boldsymbol{CB(i)}}^{\boldsymbol{(j)+}}$ (red line) of the risk index residual uncertainty computed at $\boldsymbol{k = 10}$ through the proposed procedure and compared with the risk index computed through the MLE-learned DBN $\boldsymbol{R}_{\boldsymbol{CB(i)}}^{\boldsymbol{(j)MLE}}$ (blue line) and the ground truth $\boldsymbol{R}_{\boldsymbol{CB(i)}}^{\boldsymbol{(j)GT}}$ (black line). The results are shown for the application of $\boldsymbol{a}_{\boldsymbol{(0:T)}}^{\boldsymbol{(1)}}$ (a), $\boldsymbol{a}_{\boldsymbol{(0:T)}}^{\boldsymbol{(2)}}$ (b) and $\boldsymbol{a}_{\boldsymbol{(0:T)}}^{\boldsymbol{(3)}}$ (c) for scenario 1.

Table 7. Results of the decision-making process carried out at $\boldsymbol{k = 10}$ for scenario 1.

Alternative	$\tilde{S}_{j2}$	$\tilde{F}_j$	$I_I^{\delta}(\tilde{F}_j)$ (rank)		
			Pessimistic ($\delta = 0.0$)	Moderate ($\delta = 0.5$)	Optimistic ($\delta = 1.0$)
$\boldsymbol{a}_{sp(0:T)}^{(1)}$	(0.909, 0.934, 1.000)	(0.477, 0.811, 1.000)	0.644 (2)	0.775 (2)	0.906 (2)
$\boldsymbol{a}_{sp(0:T)}^{(2)}$	(0.965, 0.991, 1.000)	(0.491, 0.830, 1.000)	0.661 (1)	0.788 (1)	0.915 (1)

$\boldsymbol{a}_{sp(0:T)}^{(3)}$	$(0.000, 0.000, 0.006)$	-	-	-	-	

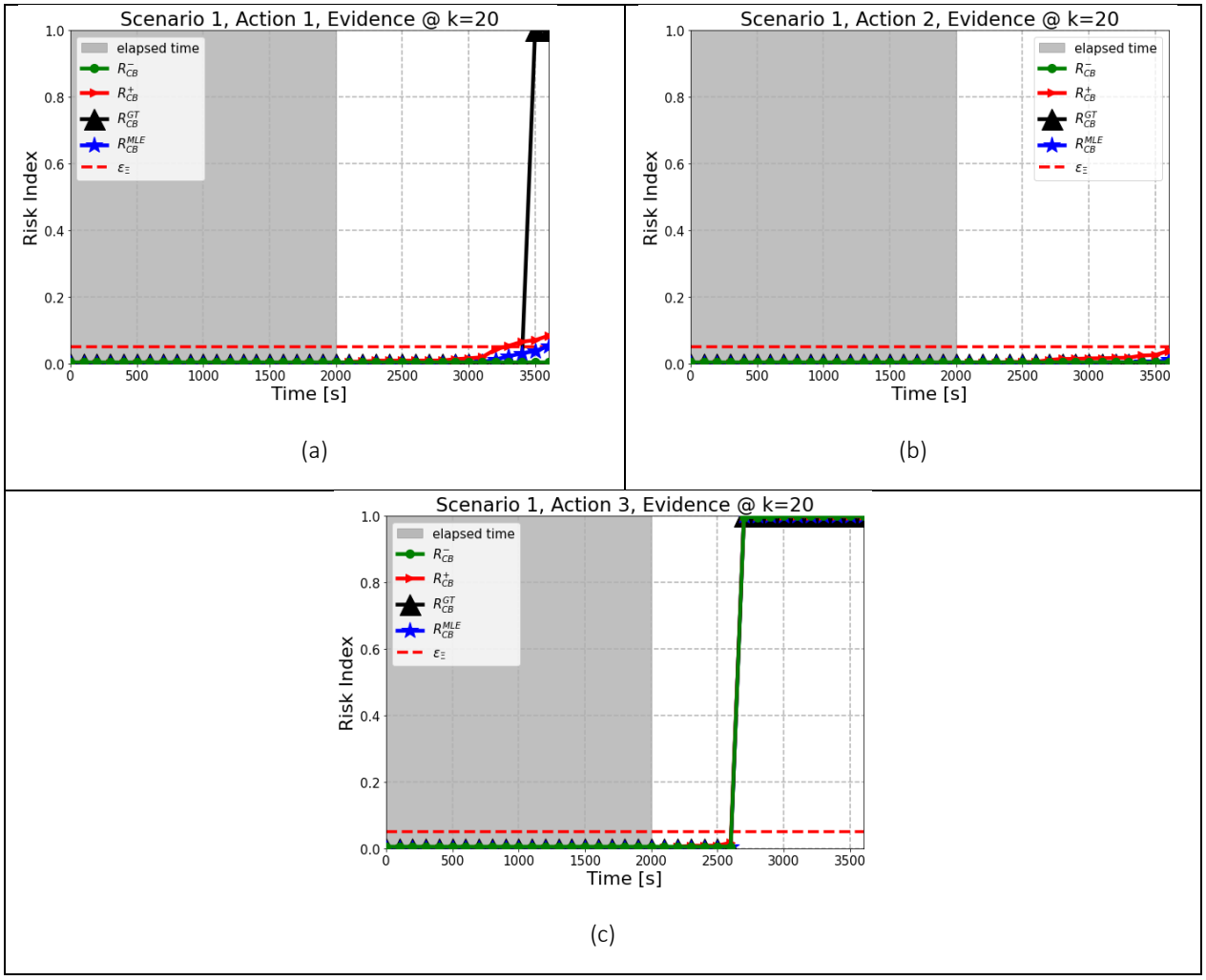

Figure 9. Lower bound $\boldsymbol{R}_{\boldsymbol{CB(i)}}^{(j)-}$ (green line) and upper bound $\boldsymbol{R}_{\boldsymbol{CB(i)}}^{(j)+}$ (red line) of the risk index residual uncertainty computed at $\boldsymbol{k = 20}$ through the proposed procedure and compared with the risk index computed through the MLE-learned DBN $\boldsymbol{R}_{\boldsymbol{CB(i)}}^{\boldsymbol{(j)MLE}}$ (blue line) and the ground truth $\boldsymbol{R}_{\boldsymbol{CB(i)}}^{\boldsymbol{(j)GT}}$ (black line). The results are shown for the application of $\boldsymbol{a}_{\boldsymbol{(0:T)}}^{\boldsymbol{(1)}}$ (a), $\boldsymbol{a}_{\boldsymbol{(0:T)}}^{\boldsymbol{(2)}}$ (b) and $\boldsymbol{a}_{\boldsymbol{(0:T)}}^{\boldsymbol{(3)}}$ (c) for scenario 1.

Table 8. Results of the decision-making process carried out at $\boldsymbol{k = 20}$ for scenario 1.

Alternative	$\tilde{S}_{j2}$	$\tilde{F}_j$	$I_T^{\delta}(\tilde{F}_j)$ (rank)		
			Pessimistic ($\delta = 0.0$)	Moderate ($\delta = 0.5$)	Optimistic ($\delta = 1.0$)
$\boldsymbol{a}_{sp(0:T)}^{(1)}$	$(0.917, 0.948, 1.000)$	$(0.479, 0.816, 1.000)$	0.648 (2)	0.778 (2)	0.908 (2)
$\boldsymbol{a}_{sp(0:T)}^{(2)}$	$(0.962, 0.989, 1.000)$	$(0.491, 0.830, 1.000)$	0.660 (1)	0.787 (1)	0.915 (1)

$\boldsymbol{a}_{sp(0:T)}^{(3)}$	$(0.00, 0.00, 0.005)$	-	-	-	-

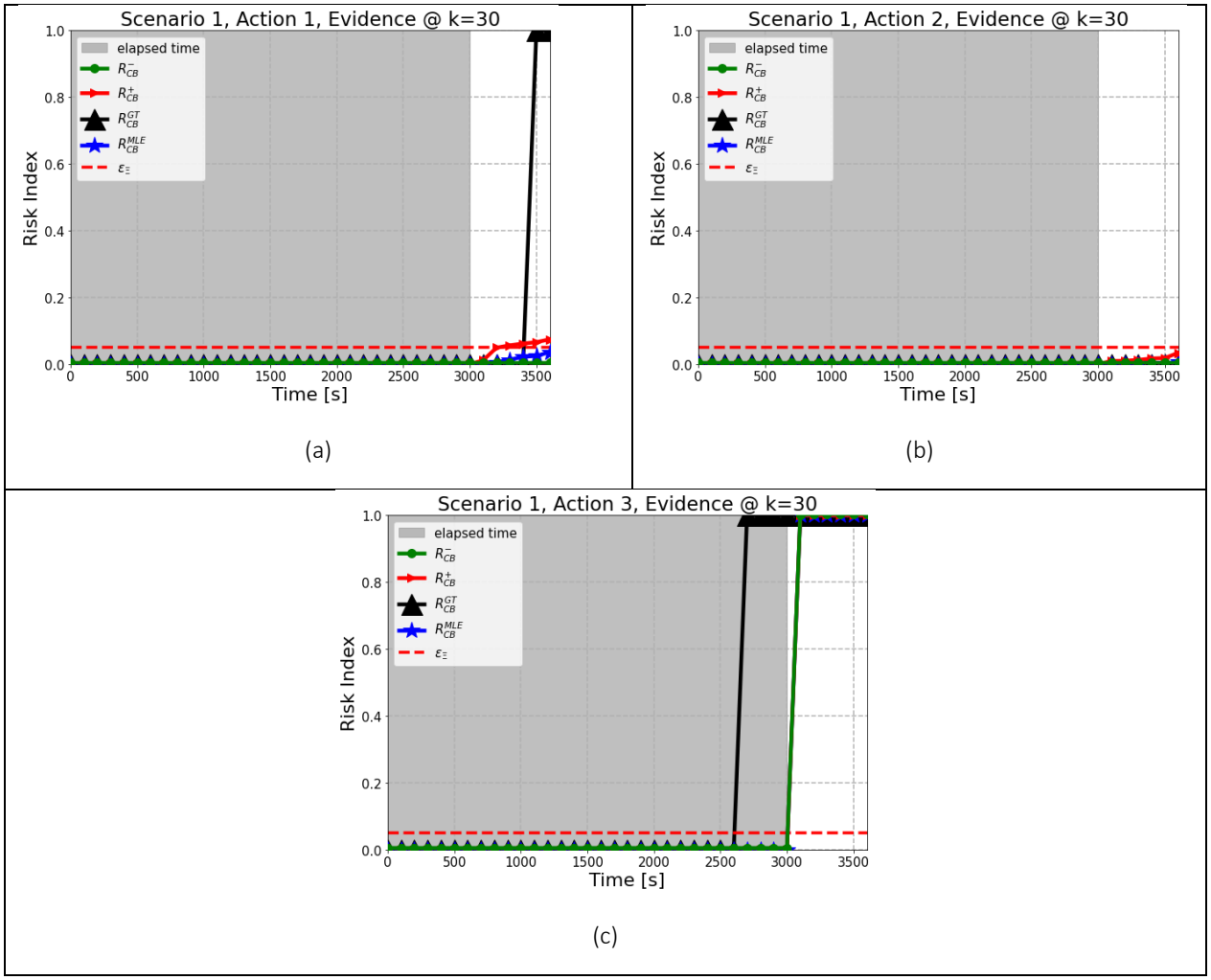

Figure 10. Lower bound $\boldsymbol{R}_{\boldsymbol{CB(i)}}^{\boldsymbol{(j)-}}$ (green line) and upper bound $\boldsymbol{R}_{\boldsymbol{CB(i)}}^{\boldsymbol{(j)+}}$ (red line) of the risk index residual uncertainty computed at $\boldsymbol{k = 30}$ through the proposed procedure and compared with the risk index computed through the MLE-learned DBN $\boldsymbol{R}_{\boldsymbol{CB(i)}}^{\boldsymbol{(j)MLE}}$ (blue line) and the ground truth $\boldsymbol{R}_{\boldsymbol{CB(i)}}^{\boldsymbol{(j)GT}}$ (black line). The results are shown for the application of $\boldsymbol{a}_{\boldsymbol{(0:T)}}^{\boldsymbol{(1)}}$ (a), $\boldsymbol{a}_{\boldsymbol{(0:T)}}^{\boldsymbol{(2)}}$ (b) and $\boldsymbol{a}_{\boldsymbol{(0:T)}}^{\boldsymbol{(3)}}$ (c) for scenario 1.

Table 9. Results of the decision-making process carried out at $\boldsymbol{k = 30}$ for scenario 1.

Alternative	$\tilde{S}_{j2}$	$\tilde{F}_j$	$I_T^{\delta}(\tilde{F}_j)$ (rank)		
			Pessimistic ($\delta = 0.0$)	Moderate ($\delta = 0.5$)	Optimistic ($\delta = 1.0$)
$\boldsymbol{a}_{sp(0:T)}^{(1)}$	$(0.926, 0.964, 1.000)$	$(0.481, 0.821, 1.000)$	0.651 (2)	0.781 (2)	0.911 (2)
$\boldsymbol{a}_{sp(0:T)}^{(2)}$	$(0.966, 0.994, 1.000)$	$(0.492, 0.831, 1.000)$	0.661 (1)	0.789 (1)	0.916 (1)
$\boldsymbol{a}_{sp(0:T)}^{(3)}$	$(0.00, 0.00, 0.001)$	-	-	-	-

4.2 Scenario 2: small LOCA with a small hydrogen production rate

Figure 11, Figure 12 and Figure 13 show the same statistics of Figure 8, Figure 9 and Figure 10 for scenario 2. We can observe that none of the mitigative actions considered lead the system to failure (i.e., $\forall i$, $R_{CB(i)}^{GT(j)} = 0$ for any action $\boldsymbol{a}_{(0:T)}^{(j)}$). However, results are trustworthy only for $\boldsymbol{a}_{(0:T)}^{(1)}$, which can also be considered effective (i.e., $\left(\max_{i>k} R_{CB(i)}^{(1)+}\right) < \epsilon_{CB}$, with $k = 10,20,30$). Conversely, the significant residual uncertainty of the risk index computed for $\boldsymbol{a}_{(0:T)}^{(2)}$ and $\boldsymbol{a}_{(0:T)}^{(3)}$ (i.e., $\left[R_{CB(i)}^{(2)-}, R_{CB(i)}^{(2)+}\right]_{\gamma}^{\beta}$ and $\left[R_{CB(i)}^{(3)-}, R_{CB(i)}^{(3)+}\right]_{\gamma}^{\beta}$) makes their effectiveness uncertain.

It is worth noticing that, while the risk index predicted through the MLE-learned DBN aligns with the ground truth for action $\boldsymbol{a}_{(0:T)}^{(1)}$ and $\boldsymbol{a}_{(0:T)}^{(2)}$ (i.e., $R_{CB(i)}^{MLE(j)} \cong 0$ for $j = 1,2$), the results for $\boldsymbol{a}_{(0:T)}^{(3)}$ do not: for evidence up to $k = 10$, $k = 20$ and $k = 30$, $R_{CB(i)}^{MLE(3)}$ exceeds ϵ_{CB} at $i = 27$, $i = 34$ and $i = 34$, respectively (Figure 11, Figure 12 and Figure 13). Thus, resorting exclusively to the MLE-learned DBN would exclude $\boldsymbol{a}_{(0:T)}^{(2)}$ and $\boldsymbol{a}_{(0:T)}^{(3)}$ from the decision making process, being $\left(\max_{i>k} R_{CB(i)}^{MLE(2)}\right) > \epsilon_{CB}$ and $\left(\max_{i>k} R_{CB(i)}^{MLE(3)}\right) > \epsilon_{CB}$, and this would represent an issue if $\boldsymbol{a}_{(0:T)}^{(1)}$ would not be feasible (e.g., because of unavailability of the spray system), because the operator would be forced to look for another mitigative action to limit the consequences of scenario 2, although unnecessarily (being $\boldsymbol{a}_{(0:T)}^{(2)}$ and $\boldsymbol{a}_{(0:T)}^{(3)}$ effective). Thus, adopting a standard approach for CPTs parameters learning (e.g., MLE-based), which provides only point estimates of CPTs parameters, can lead decision makers to selecting incorrect conclusions.

Table 10, Table 11 and Table 12 present the results of the decision-making process carried out for scenario 2 at $k = 10, 20, 30$, respectively. As in scenario 1, the ranking of the best decision alternative is determined solely by its *Effectiveness*, which is assessed using the DBN, since all decision alternatives are considered equally *Feasible* and *Compatible* (see Table 6). As expected, $\boldsymbol{a}_{sp_{(0:T)}}^{(1)}$ is ranked as the best sequence of actions, except for $k = 30$, where the condition $\left(\max_{i>k} R_{CB(i)}^{(1)MLE}\right) > \left(\max_{i>k} R_{CB(i)}^{(2)MLE}\right)$ holds, leading to $b_{\tilde{s}_{12}} < b_{\tilde{s}_{22}}$ and, thus, $I_T^{\delta}\left(\tilde{F}_2\right) > I_T^{\delta}\left(\tilde{F}_1\right)$.

As expected, $\boldsymbol{a}_{sp_{(0:T)}}^{(1)}$ is ranked as the best action among the alternatives, except for $k = 20$ and $k = 30$: in these cases, for $\delta = 1.0$, $\boldsymbol{a}_{sp_{(0:T)}}^{(2)}$ is to be preferred to $\boldsymbol{a}_{sp_{(0:T)}}^{(1)}$. However, considering the severity of the consequences of a CB failure, the ranking with $\delta = 1.0$ is to be discarded (with $\delta = 1.0$, the contribution of $d_{\tilde{s}_{j2}}$, being multiplied by zero (i.e., $(1-\delta)$), is neglected and $\left(\max_{i>k} R_{CB(i)}^{(1)MLE}\right) > \left(\max_{i>k} R_{CB(i)}^{(2)MLE}\right)$ leads to $b_{\tilde{s}_{12}} < b_{\tilde{s}_{22}}$ and, thus, $I_T^{\delta=1}\left(\tilde{F}_2\right) > I_T^{\delta=1}\left(\tilde{F}_1\right)$).

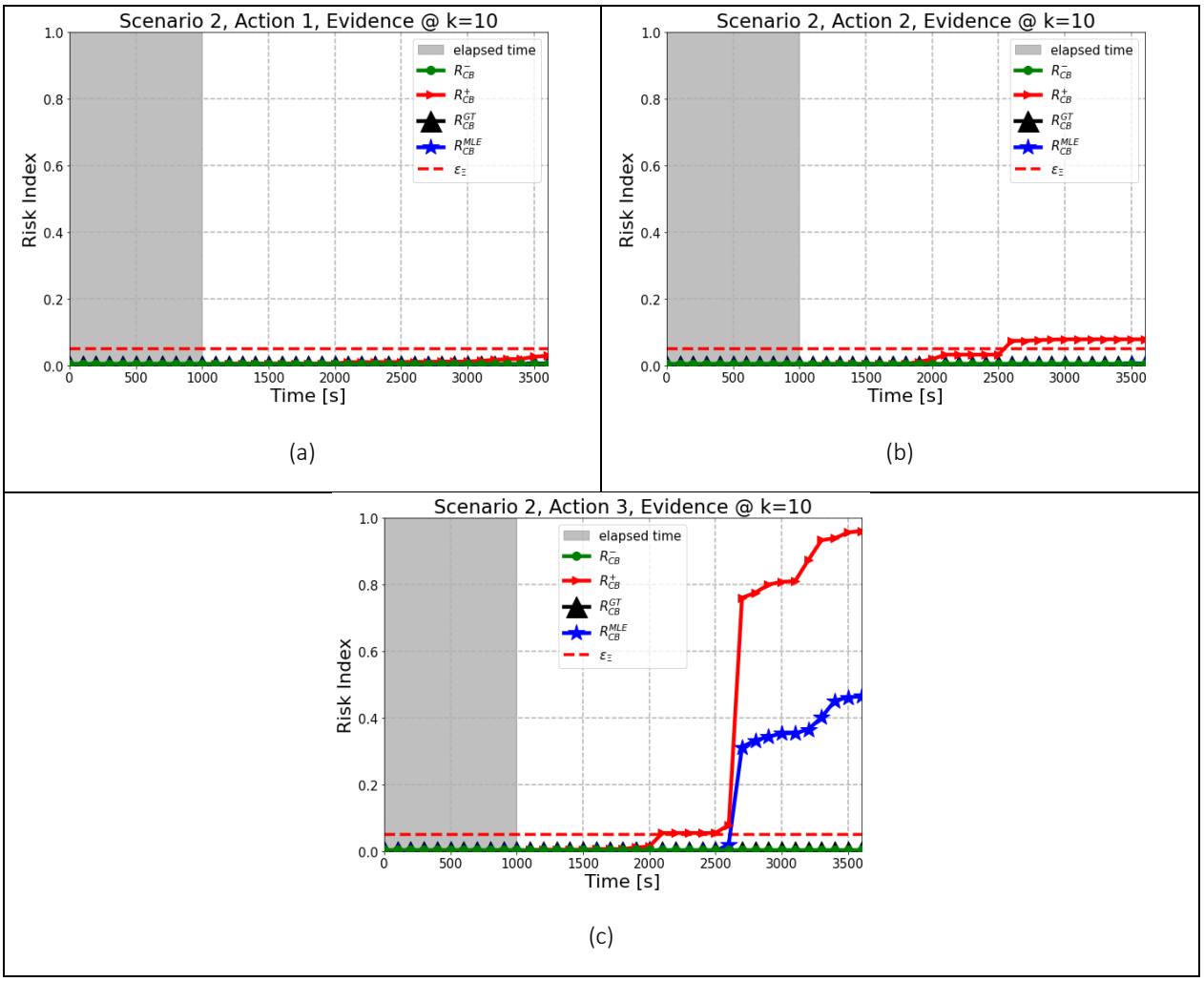

Figure 11. Lower bound $\boldsymbol{R}_{\boldsymbol{CB}(\boldsymbol{i})}^{(\boldsymbol{j})-}$ (green line) and upper bound $\boldsymbol{R}_{\boldsymbol{CB}(\boldsymbol{i})}^{(\boldsymbol{j})+}$ (red line) of the risk index residual uncertainty computed at $\boldsymbol{k} = \mathbf{10}$ through the proposed procedure and compared with the risk index computed through the MLE-learned DBN $\boldsymbol{R}_{\boldsymbol{CB}(\boldsymbol{i})}^{(\boldsymbol{j})\boldsymbol{MLE}}$ (blue line) and the ground truth $\boldsymbol{R}_{\boldsymbol{CB}(\boldsymbol{i})}^{(\boldsymbol{j})\boldsymbol{GT}}$ (black line). The results are shown for the application of $\boldsymbol{a}_{(\mathbf{0}:\boldsymbol{T})}^{(\mathbf{1})}$ (a), $\boldsymbol{a}_{(\mathbf{0}:\boldsymbol{T})}^{(\mathbf{2})}$ (b) and $\boldsymbol{a}_{(\mathbf{0}:\boldsymbol{T})}^{(\mathbf{3})}$ (c) for scenario 2.

Table 10. Results of the decision-making process carried out at k=10 for scenario 2.

Alternative	$\tilde{S}_{j2}$	$\tilde{F}_j$	$I_T^{\delta}(\tilde{F}_j)$ (rank)		
			Pessimistic ($\delta = 0.0$)	Moderate ($\delta = 0.5$)	Optimistic ($\delta = 1.0$)
$\boldsymbol{a}_{sp(0:T)}^{(1)}$	$(0.971, 0.994, 1.000)$	$(0.493, 0.831, 1.000)$	0.662 (1)	0.789 (1)	0.916 (1)
$\boldsymbol{a}_{sp(0:T)}^{(2)}$	$(0.921, 0.994, 1.000)$	$(0.480, 0.832, 1.000)$	0.656 (2)	0.786 (2)	0.916 (2)
$\boldsymbol{a}_{sp(0:T)}^{(3)}$	$(0.039, 0.535, 1.000)$	$(0.260, 0.678, 1.000)$	0.469(3)	0.654 (3)	0.839 (3)

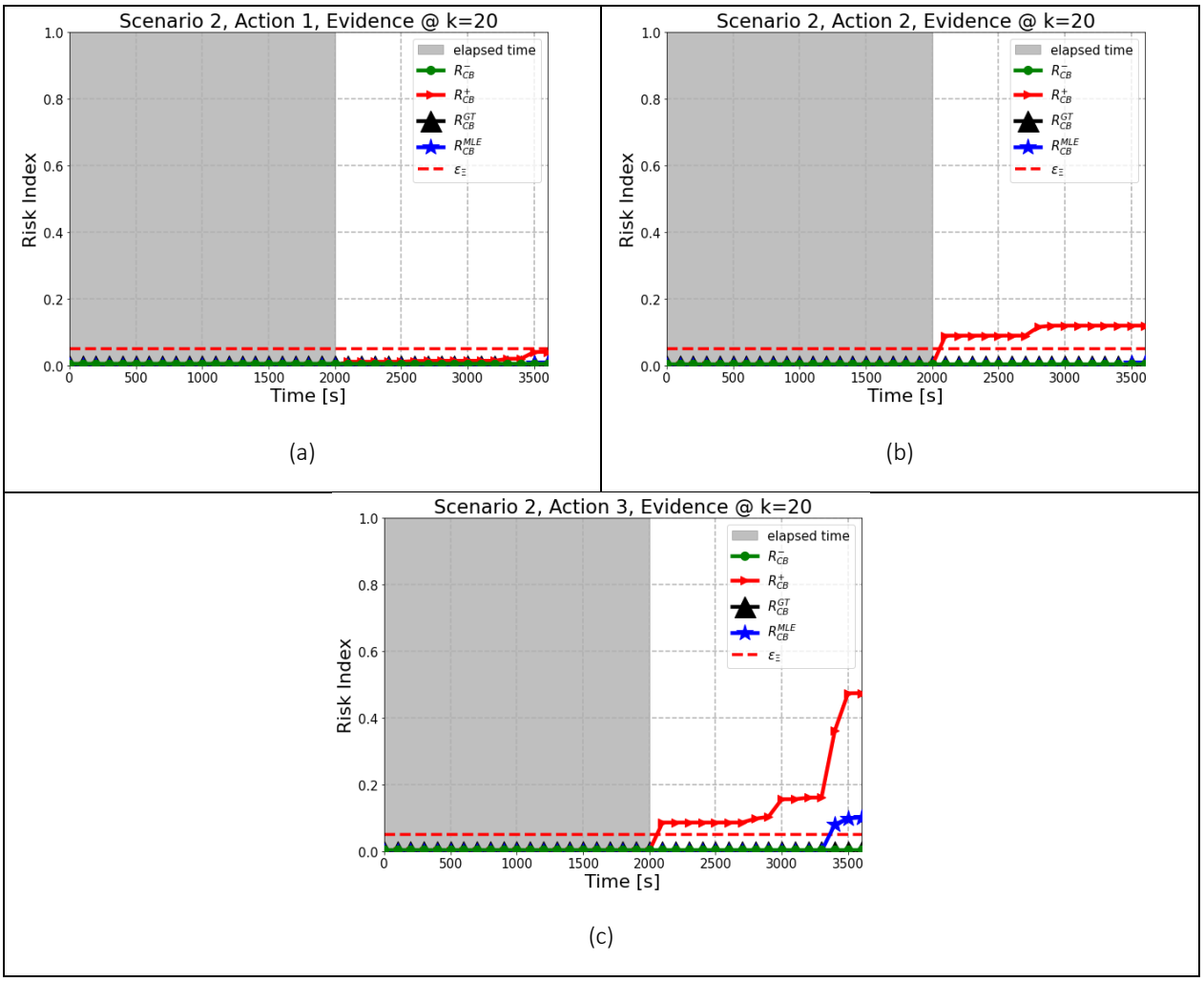

Figure 12. Lower bound $\boldsymbol{R}_{\boldsymbol{CB}(\boldsymbol{i})}^{(\boldsymbol{j})-}$ (green line) and upper bound $\boldsymbol{R}_{\boldsymbol{CB}(\boldsymbol{i})}^{(\boldsymbol{j})+}$ (red line) of the risk index residual uncertainty computed at $\boldsymbol{k} = \boldsymbol{20}$ through the proposed procedure and compared with the risk index computed through the MLE-learned DBN $\boldsymbol{R}_{\boldsymbol{CB}(\boldsymbol{i})}^{(\boldsymbol{j})\boldsymbol{MLE}}$ (blue line) and the ground truth $\boldsymbol{R}_{\boldsymbol{CB}(\boldsymbol{i})}^{(\boldsymbol{j})\boldsymbol{GT}}$ (black line). The results are shown for the application of $\boldsymbol{a}_{(\boldsymbol{0}:\boldsymbol{T})}^{(\boldsymbol{1})}$ (a), $\boldsymbol{a}_{(\boldsymbol{0}:\boldsymbol{T})}^{(\boldsymbol{2})}$ (b) and $\boldsymbol{a}_{(\boldsymbol{0}:\boldsymbol{T})}^{(\boldsymbol{3})}$ (c) for scenario 2.

Table 11. Results of the decision-making process carried out at k=20 for scenario 2.

Alternative	$\tilde{S}_{j2}$	$\tilde{F}_j$	$I_T^{\delta}(\tilde{F}_j)$ (rank)		
			Pessimistic ($\delta = 0.0$)	Moderate ($\delta = 0.5$)	Optimistic ($\delta = 1.0$)
$\boldsymbol{a}_{sp(0:T)}^{(1)}$	$(0.959, 0.992, 1.000)$	$(0.490, 0.831, 1.000)$	0.660 (1)	0.788 (1)	0.915 (2)
$\boldsymbol{a}_{sp(0:T)}^{(2)}$	$(0.881, 0.994, 1.000)$	$(0.470, 0.831, 1.000)$	0.651(2)	0.783 (2)	0.916 (1)
$\boldsymbol{a}_{sp(0:T)}^{(3)}$	$(0.525, 0.899, 1.000)$	$(0.381, 0.800, 1.000)$	0.590 (3)	0.745 (3)	0.900 (3)

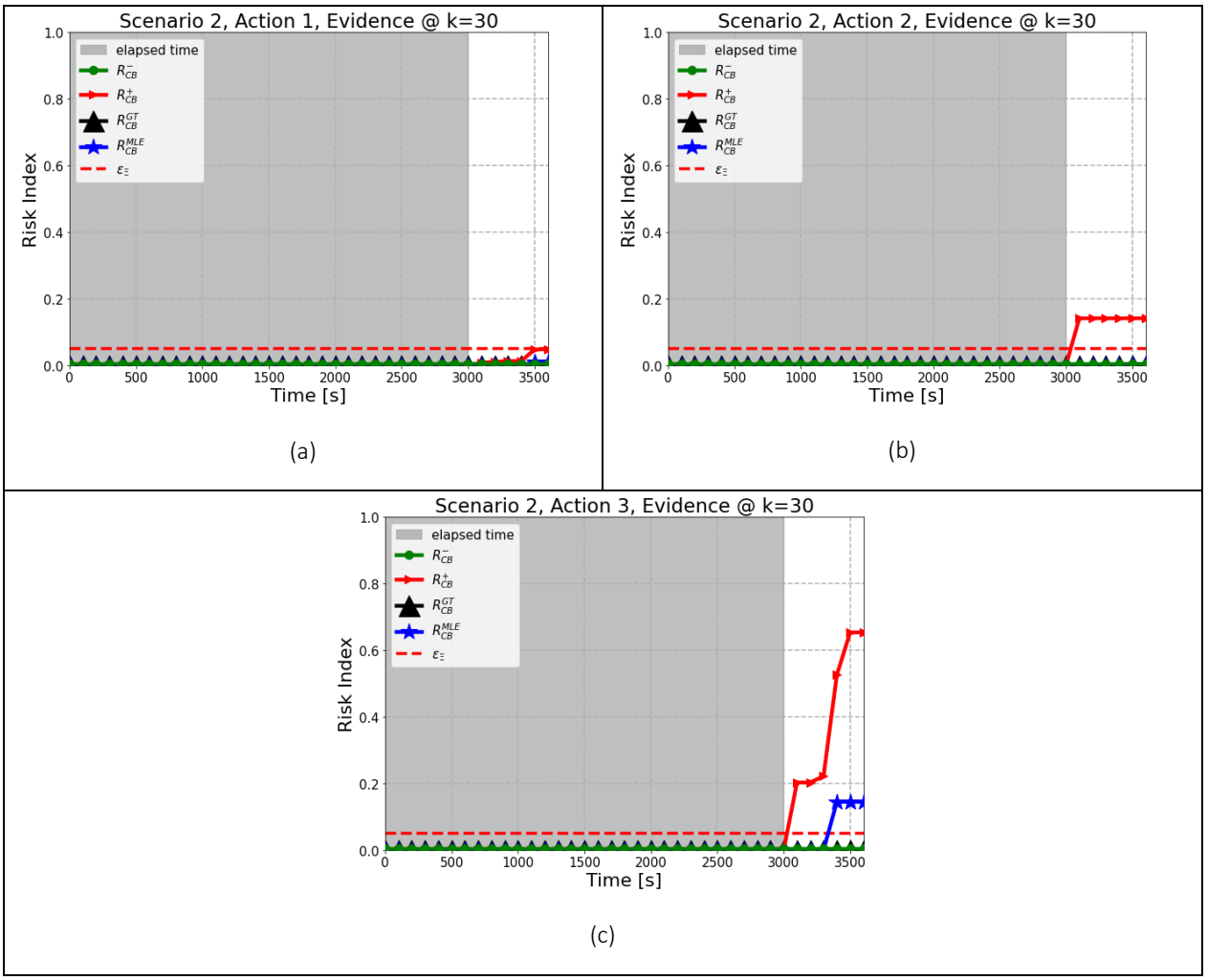

Figure 13. Lower bound $\boldsymbol{R}_{\boldsymbol{CB}(\boldsymbol{i})}^{(\boldsymbol{j})-}$ (green line) and upper bound $\boldsymbol{R}_{\boldsymbol{CB}(\boldsymbol{i})}^{(\boldsymbol{j})+}$ (red line) of the risk index residual uncertainty computed at $\boldsymbol{k} = \mathbf{30}$ through the proposed procedure and compared with the risk index computed through the MLE-learned DBN $\boldsymbol{R}_{\boldsymbol{CB}(\boldsymbol{i})}^{(\boldsymbol{j})\boldsymbol{MLE}}$ (blue line) and the ground truth $\boldsymbol{R}_{\boldsymbol{CB}(\boldsymbol{i})}^{(\boldsymbol{j})\boldsymbol{GT}}$ (black line). The results are shown for the application of $\boldsymbol{a}_{(\mathbf{0}:\boldsymbol{T})}^{(\mathbf{1})}$ (a), $\boldsymbol{a}_{(\mathbf{0}:\boldsymbol{T})}^{(\mathbf{2})}$ (b) and $\boldsymbol{a}_{(\mathbf{0}:\boldsymbol{T})}^{(\mathbf{3})}$ (c) for scenario 2.

.

Table 12. Results of the decision-making process carried out at k=30 for scenario 2.

Alternative	$\tilde{S}_{j2}$	$\tilde{F}_j$	$I_T^{\delta}(\tilde{F}_j)$ (rank)		
			Pessimistic ($\delta = 0.0$)	Moderate ($\delta = 0.5$)	Optimistic ($\delta = 1.0$)
$\boldsymbol{a}_{sp(0:T)}^{(1)}$	(0.952, 0.990, 1.000)	(0.488, 0.830, 1.000)	0.659 (1)	0.787 (1)	0.915 (2)
$\boldsymbol{a}_{sp(0:T)}^{(2)}$	(0.859, 0.997, 1.000)	(0.465, 0.832, 1.000)	0.649 (2)	0.782 (2)	0.916 (1)
$\boldsymbol{a}_{sp(0:T)}^{(3)}$	(0.346, 0.855, 1.000)	(0.337, 0.785, 1.000)	0.561 (3)	0.727 (3)	0.893 (3)

Let us now assume that the decision maker assigns very high importance to *feasibility* and *effectiveness*, and medium importance to *compatibility* (see Table 13). At $k = 10$, *feasibility* is low for $\boldsymbol{a}_{sp(0:T)}^{(1)}$ (early activation), high for $\boldsymbol{a}_{sp(0:T)}^{(2)}$ (delayed activation), and very high for $\boldsymbol{a}_{sp(0:T)}^{(3)}$ (no activation)(see Table 14), reflecting, for instance, the case that the spray system may not be prompt for activation (e.g., under maintenance), but likely to become available as time progresses. Conversely, c*ompatibility* is high for $\boldsymbol{a}_{sp(0:T)}^{(1)}$, low for $\boldsymbol{a}_{sp(0:T)}^{(2)}$, and very low for $\boldsymbol{a}_{sp(0:T)}^{(3)}$ (see Table 14), consistently with SAMG guidance, which advises delaying or limiting sprays only when the atmosphere approaches flammability. *Effectiveness* is the same as in Tables 10–12. The results at $k = 10$ (Table 15) show that $\boldsymbol{a}_{sp(0:T)}^{(2)}$, rather than $\boldsymbol{a}_{sp(0:T)}^{(1)}$, is the highest-ranked alternative and, thus, should be preferred.

Table 13. Linguistic variables (and corresponding TFNs) assigned to the criteria importance weights for the alternative decision-making settings.

Criterion	Importance weight ($\widetilde{W}_\lambda$)
Feasibility	Very High $(0.75, 1, 1)$
Effectiveness	Very High $(0.75, 1, 1)$
Compatibility	Medium $(0.25, 0.5, 0.75)$

Table 14. Linguistic variables (and corresponding TFNs) assigned at $\boldsymbol{k = 10}$ to the decision alternatives with respect to Feasibility and Compatibility for the alternative decision-making settings.

Alternatives	*Feasibility* ($\tilde{S}_{j1}$)	*Compatibility* ($\tilde{S}_{j3}$)
$\boldsymbol{a}_{sp(0:T)}^{(1)}$	Low $(0, 0.25, 0.5)$	High $(0.5, 0.75, 1)$
$\boldsymbol{a}_{sp(0:T)}^{(2)}$	High $(0.5, 0.75, 1)$	Low $(0, 0.25, 0.5)$
$\boldsymbol{a}_{sp(0:T)}^{(3)}$	Very High $(0.75, 1, 1)$	Very Low $(0, 0, 0.25)$

Table 15. Results of the decision-making process carried out at k=10 for the alternative decision-making settings.

Alternative	$\tilde{S}_{j2}$	$\tilde{F}_j$	$I_T^{\delta}(\tilde{F}_j)$ (rank)		
			Pessimistic ($\delta = 0.0$)	Moderate ($\delta = 0.5$)	Optimistic ($\delta = 1.0$)
$\boldsymbol{a}_{sp(0:T)}^{(1)}$	$(0.971, 0.994, 1.000)$	$(0.284, 0.540, 0.750)$	0.412 (2)	0.528 (2)	0.645 (2)
$\boldsymbol{a}_{sp(0:T)}^{(2)}$	$(0.921, 0.994, 1.000)$	$(0.355, 0.624, 0.792)$	0.490 (1)	0.599 (1)	0.708 (1)
$\boldsymbol{a}_{sp(0:T)}^{(3)}$	$(0.039, 0.535, 1.000)$	$(0.197, 0.512, 0.729)$	0.354 (3)	0.487 (3)	0.620 (3)

5 Conclusions

This paper proposes a methodological framework of DBN-based AMST for assisting decisions regarding the best sequence of mitigative actions to undertake during a NPP severe accident. The DBN-based AMST consists of four main modules: a state estimation module, a risk predictor module, a trustworthiness assessment module and a decision-making module. Both the state estimation and the risk predictor modules employ a DBN. The state estimation module infers the PDS probability distribution from real-time sensor data. The risk predictor module quantifies the consequences of deploying the candidate sequences of mitigative actions by predicting user-defined time-dependent risk indices. The trustworthiness assessment module evaluates the epistemic uncertainty affecting the outcomes provided by the risk predictor module using non-parametric tolerance intervals. Trustworthiness is ensured if either the risk index residual uncertainty is entirely below the acceptable risk limit set by the decision-maker and/or regulatory body, or entirely above the risk limit for some time instances (i.e., the sequence of action is assessed as non-effective for the specific scenario developing). The decision-making module integrates expert judgment with the results of the trustworthiness assessment module, using (without loss of generality and only for exemplification purpose) a fuzzy logic multi-criteria approach to select the best sequence of mitigative actions.

An application is presented with regards to a LOCA in a realistic WWER-1000, for which three alternative actions (i.e., early, delayed and no activation of the spray system) are considered to mitigate CB damage. The results show that adopting a standard approach for CPTs parameters learning (e.g., MLE-based), which provides only point estimates, can lead decision makers to selecting incorrect actions.

For applicability of the proposed framework in practice, the following aspects need to be considered:

- DBN training data: field/experimental data of severe accidents are limited and, thus, simulation data must be generated for training the DBN, ensuring that all severe accident phenomena and their uncertainties are duly considered in the models used for the simulation.
- DBN modelling assumptions: the residual uncertainty due to the DBN structure and continuous variables discretization is neglected. Future work will explore the use of:
    - causal discovery approaches [52,53] for the identification of causal relationships from data, so that the structure uncertainty is properly handled, and
    - Hybrid Bayesian Networks [54] to avoid the discretization of the continuous variables.
- DBN computational time: the computational demand increases with the complexity of the DBN [55]. Future work will investigate methods of propagation of CPTs parameter uncertainty more efficient than standard Monte Carlo.
- Scope of the analysis: a plant full-scope safety analysis should consider a large number of initiating events, plant operating conditions and SAM actions (e.g., filtered containment venting and combined strategies), and compute a comprehensive set of risk indices (e.g., LERF).
- Sensors reliability/availability: during severe accidents, harsh conditions (e.g., high temperature, pressures and radiation levels) can impair the reliability/availability of the measurements. Future work will deal with the uncertain evidence coming from unreliable measurements.
- Sequential SAM actions: in this work a single safety system (spray under LOCA) is considered and, thus, few alternative actions evaluated. The DBN-based AMST proposed is, however, applicable to sequential SAM actions (i.e., the activation of multiple mitigative safety barriers during the accident evolution). Future work will address the dependence between multiple, successive decisions and actions.

6 Appendix A

6.1 CPTs parameters uncertainty quantification and propagation

Methods for characterizing the uncertainty of CPTs parameters are either based on *probability* theory or on *interval-valued* uncertainty [56]. The former assumes that the uncertainty on CPTs parameters follows a Dirichlet probability distribution (or a Beta distribution for binary nodes) and then propagate this uncertainty, typically through Monte Carlo sampling, to characterize the residual uncertainty (i.e., Eqs. (3) in this paper); the latter (also referred as methods based on Credal Networks) assumes that the uncertainty

in the CPTs is presented by intervals and then propagates this uncertainty to characterize the residual uncertainty about the considered query by solving optimization problems over the sets of probabilities [56]. However, although Credal Networks constitutes a systematic methodology for representing and propagating CPTs uncertainty, the computational complexity and, therefore, the computational time required for the inference process can be intractable for complex networks (i.e., networks characterized by a large number of nodes and high treewidth) [57,58]; for this reason, in this work, we opt for the former category of methods.

Section 6.1.1 shows how to quantify the CPTs parameters uncertainty, whereas Section 6.1.2 shows how to propagate it to find $\left[R_{\xi(i)}^{(j)-}, R_{\xi(i)}^{(j)+}\right]_{\gamma}^{\beta}$ by probability theory.

6.1.1 CPTs parameters uncertainty quantification

A popular approach to quantify the uncertainty about CPTs parameters is to use Bayesian inference, in which a Dirichlet (i.e., a conjugate) prior $\boldsymbol{\theta}_{nm} \sim D(\alpha_{nm1}, \dots, \alpha_{nmc_n})$ is typically assigned to the CPTs parameters:

$$p(\theta_{nm1}, \dots, \theta_{nmc_n} | \alpha_{nm1}, \dots, \alpha_{nmc_n}) = \frac{1}{\beta(\alpha_{nm1}, \dots, \alpha_{nmc_n})} \prod_{u=1}^{c_n} \theta_{nmu}^{\alpha_{nmu}-1} \tag{A.1}$$

where $\beta(\alpha_{nm1}, \dots, \alpha_{nmc_n})$ is the c_n-dimensional Beta function:

$$\beta(\alpha_{nm1}, \dots, \alpha_{nmc_n}) = \frac{\prod_{u=1}^{c_n} \Gamma(\alpha_{nmu})}{\Gamma\left(\sum_{u=1}^{c_n} \alpha_{nmu}\right)} \tag{A.2}$$

where $\Gamma(\cdot)$ is the gamma function, for positive integers, $\Gamma(n) = (n-1)!$

The prior hyperparameters, $\alpha_{nmu} > 0$, can be interpreted as pseudo-counts (i.e., the quantity α_{nmu} represents the number of times the expert believes he/she will observe the event $(Z_n = u | Pa(Z_n) = m)$ in a virtual prior learning dataset). The prior distribution is then updated using $\boldsymbol{\mathcal{D}}$, so the posterior distribution becomes $\boldsymbol{\theta}_{nm} | \boldsymbol{\mathcal{D}} \sim D(\alpha_{nm1} + N_{nm1}, \dots, \alpha_{nmc_n} + N_{nmc_n})$. Thus, the posterior mean is

$$E[\theta_{nmu} | \boldsymbol{\mathcal{D}}] = \frac{\alpha_{nmu} + N_{nmu}}{\sum_{u=1}^{n_c} \alpha_{nmu} + N_{nmu}} \tag{A.3}$$

and the posterior mode (MAP estimate) is

$$\operatorname{argmax} p(\theta_{nmu} | \boldsymbol{\mathcal{D}}) = \frac{\alpha_{nmu} + N_{nmu} - 1}{\sum_{u=1}^{n_c} \alpha_{nmu} + N_{nmu} - c_n} \tag{A.4}$$

When the number of observed samples in $\boldsymbol{\mathcal{D}}$ is very large, (i.e., $\sum_{u=1}^{c_n} N_{nmu} \gg 1$), the contribution of the prior is negligible, and the posterior mean and MAP estimate align with the MLE. Similarly, for $\alpha_{nm} = \sum_{u=1}^{n_c} \alpha_{nmu} \to 0$ the posterior mean converges to the MLE because it relies entirely on observed data, with no additional prior information affecting the result. The prior with any $\alpha_{nmu} = 0$ is an *improper* prior (i.e.,

it does not integrate to a finite value), and it causes the posterior log-likelihood to explode if also $N_{nmu} = 0$. Following Heckerman et al. [59], in in this work we adopt the uninformative uniform prior $\alpha_{nmu} = \frac{\alpha}{c_n d_n}$ which, in the case of scarce prior knowledge, should be preferred instead of an informative (but incorrect) prior. The equivalent sample size α is typically set by the user and it represents the number of observations that would be needed to achieve the same level of confidence in the CPTs prior hyperparameters as the user currently possesses; thus, it is not a measure of actual data but reflects the strength of the user prior beliefs. The selection of α is out of purpose of this paper and the interested reader may refer to [59] for more insights.

6.1.2 CPTs parameters uncertainty propagation

After developing the DBN and characterizing the uncertainty of the CPTs parameters uncertainty through the posterior distribution $\boldsymbol{\theta}_{nm}|\boldsymbol{\mathcal{D}} \sim D(\alpha_{nm1} + N_{nm1}, \dots, \alpha_{nmc_n} + N_{nmc_n})$, the residual uncertainty in the risk indices is characterized through the non-parametric tolerance interval $\left[R_{\xi(i)}^{(j)-}, R_{\xi(i)}^{(j)+}\right]_{\gamma}^{\beta}$. To calculate N_{γ}^{β}, which is the number of samples from the (unknown) probability distribution $p\left(R_{\xi(i)}^{(j)}\right)$ needed to ensure that $\left[R_{\xi(i)}^{(j)-}, R_{\xi(i)}^{(j)+}\right]_{\gamma}^{\beta}$ achieves at least the coverage γ with a confidence β, we apply Wilks formula [49]:

$$\beta = 1 - \gamma^{N_{\gamma}^{\beta}} - \left(N_{\gamma}^{\beta} - 1\right)(1-\gamma)\gamma^{N_{\gamma}^{\beta}-1} \tag{A.5}$$

where $R_{\xi(i)}^{(j)-}$ and $R_{\xi(i)}^{(j)+}$ are the minimum and the maximum of the N_{γ}^{β} values sampled from $p\left(R_{\xi(i)}^{(j)}\right)$, respectively. In particular, the values of $R_{\xi(i)}^{(j)-}$ and $R_{\xi(i)}^{(j)+}$ are determined through the following algorithm, executed at each time step $k = 1, \dots T-1$:

1. Set evidence on the observed nodes (i.e., $\boldsymbol{\phi} = \boldsymbol{\varphi};\ \boldsymbol{Y}_{(0:k)} = \boldsymbol{y}_{(0:k)}$);
2. Set the action nodes according to the sequence of future actions to be analyzed (i.e., $\boldsymbol{A}_{(k+1:T)} = \boldsymbol{a}_{(k+1:T)}^{(j)}$);
3. For $\nu = 1, \dots, N_{\gamma}^{\beta}$
   i. Sample all the CPTs parameters from $\boldsymbol{\theta}_{nm}|\boldsymbol{\mathcal{D}} \sim D(\alpha_{nm1} + N_{nm1}, \dots, \alpha_{nmc_n} + N_{nmc_n})$ and update the CPTs accordingly;
   ii. Perform DBN inference by computing $R_{\xi(i)}^{(j)}(\nu)$ for each $\boldsymbol{a}_{(k+1:T)}^{(j)}$, $i > k$ and $\xi = 1,2, \dots, \Xi$;
4. Find $R_{\xi(i)}^{(j)-} = \min\left(R_{\xi(i)}^{(j)}(1), \dots, R_{\xi(i)}^{(j)}(N_{\gamma}^{\beta})\right)$ and $R_{\xi(i)}^{(j)+} = \max\left(R_{\xi(i)}^{(j)}(1), \dots, R_{\xi(i)}^{(j)}(N_{\gamma}^{\beta})\right)$.

7 Appendix B

7.1 Primary circuit model

The primary circuit of the RCS is modeled by a zero-dimensional (0-D) approach, where the principles of mass and energy conservation are applied to determine the variables representative for the entire primary circuit: water pressure $p_p(t)$, temperature $T_p(t)$ and void fraction $\alpha_p(t)$:

$$\alpha_p = \frac{V_g}{V_f + V_g} \tag{B.1}$$

where V_f is the volume occupied by the saturated water and V_g is the volume occupied by the saturated steam. Specifically, the RCS is modelled as an ideal pressurized vessel having volume $V_p = V_f + V_g$ and characterized by a bottom break with area $BS = \pi r_{BS}^2$ from which the flowrate $\dot{m}_{BR}(t)$ spills out and is released into the CB with specific enthalpy $h_{BR}(t)$. Both $\dot{m}_{BR}(t)$ and $h_{BR}(t)$ are determined through a homogeneous equilibrium model [41] which takes as input $p_p(t)$, $T_p(t)$, and $\alpha_p(t)$ and provides as output:

$$\dot{m}_{BR}(t) = \begin{cases} \dot{m}_{BR}\left(p_p(t), T_p(t)\right) & \text{subcooled conditions} \\ \dot{m}_{BR}\left(p_p(t), \alpha_p(t)\right) & \text{saturated conditions} \end{cases} \tag{B.2}$$

$$h_{BR}(t) = \begin{cases} h_{BR}\left(p_p(t), T_p(t)\right) & \text{subcooled conditions} \\ h_{BR}\left(p_p(t), \alpha_p(t)\right) & \text{saturated conditions} \end{cases} \tag{B.3}$$

If we assume the primary circuit water to be in subcooled conditions at $t = 0$, $\alpha_p(0) = 0$ and the mass and energy balance for the control volume, coinciding with the primary circuit boundary, can be written as:

$$\dot{m}_{BR} + \dot{m}_{l,p} = 0 \tag{B.4}$$

$$\dot{m}_{BR} h_{BR} + \dot{U}_{l,p} = 0 \tag{B.5}$$

where $\dot{m}_{l,p}$ and $\dot{U}_{l,p}$ are the temporal derivatives of the liquid water mass and internal energy of the primary circuit, respectively. The mass of water in the primary circuit $m_{l,p}$ can be written as a function of the primary circuit volume V_p and the liquid density $\rho_{l,p} = \rho_l(p_p, T_p)$:

$$m_{l,p} = V_p \rho_{l,p} \tag{B.6}$$

and $U_{l,p}$ can be written as:

$$U_{l,p} = V_p \rho_{l,p} u_{l,p} \tag{B.7}$$

where the specific internal energy $u_{l,p}$ is:

$$u_{l,p} = h_{l,p} - p_p v_{l,p} \tag{B.8}$$

and $h_{l,p} = h_l\left(p_p, T_p\right)$ is the specific enthalpy of the liquid water.

Considering the primary circuit boundary non-deformable (i.e., $\dot{V}_p = 0$) and substituting Eqs. (B.6-B.8) into Eqs. (B.4-B.5), we rewrite these latter in matrix form:

$$\begin{bmatrix} V_p \frac{\partial \rho_{l,p}}{\partial p_p} & V_p \frac{\partial \rho_{l,p}}{\partial T_p} \\ V_p \left[\frac{\partial \rho_{l,p}}{\partial p_p} \left(h_{l,p} - p_p v_{l,p} \right) + \rho_l \frac{\partial h_l, p}{\partial p_p} - 1 \right] & V_p \left[\frac{\partial \rho_{l,p}}{\partial T_p} \left(h_{l,p} - p_p v_{l,p} \right) + \rho_l \frac{\partial h_{l,p}}{\partial T_p} \right] \end{bmatrix} \begin{bmatrix} \dot{p_p} \\ \dot{T_p} \end{bmatrix} = \begin{bmatrix} -\dot{m}_{BR} \\ -\dot{m}_{BR} h_{BR} \end{bmatrix} \quad \text{(B.9)}$$

where $v_l = v_l(p_p, T_p)$ is the specific volume of the liquid water.

After the break, the pressure in the primary circuit decreases, and the water reaches saturation conditions causing $\alpha_p(t) > 0$. The thermodynamic properties of the primary circuit water in saturation conditions depend on $p_p(t)$ and $\alpha_p(t)$, thus, the mass and the energy balance are written as:

$$\dot{m}_{BR} + V_p \frac{d}{dt} \left[(1 - \alpha_p) \rho_{f,p} + \alpha_p \rho_{g,p} \right] = 0 \quad \text{(B.10)}$$

$$V_p \frac{d}{dt} \left[(1 - \alpha_p) \rho_{f,p} u_{f,p} + \alpha_p \rho_{g,p} u_{g,p} \right] + \dot{m}_{BR} h_{BR} = 0 \quad \text{(B.11)}$$

where the subscripts f and g refer to the saturated liquid and saturated steam conditions, respectively. Similarly to the subcooled case, equations (B.10-B.11) are rearranged in matrix form:

$$\begin{bmatrix} V_p \left[(1 - \alpha_p) \frac{\partial \rho_{f,p}}{\partial p_p} + \alpha_p \frac{\partial \rho_{g,p}}{\partial p_p} \right] & V_p \left[-\rho_{f,p} + \rho_{g,p} \right] \\ V_p \left\{ (1 - \alpha_p) \left[h_{f,p} \frac{\partial \rho_{f,p}}{\partial p_p} + \rho_{f,p} \frac{\partial h_{f,p}}{\partial p_p} \right] + \alpha_p \left[h_{g,p} \frac{\partial \rho_{g,p}}{\partial p_p} + \rho_{g,p} \frac{\partial h_{g,p}}{\partial p_p} \right] - 1 \right\} & V_p \left[-\rho_{f,p} h_{f,p} + \rho_{g,p} h_{g,p} \right] \end{bmatrix} \begin{bmatrix} \dot{p_p} \\ \dot{\alpha_p} \end{bmatrix} = \begin{bmatrix} -\dot{m}_{BR} \\ -\dot{m}_{BR} h_{BR} \end{bmatrix} \quad \text{(B.12)}$$

By setting the initial conditions according to Table 2 and solving the system of differential equations (B.9) (if the water in the primary circuit is in subcooled conditions) and (B.12) (if it is in saturated conditions) jointly with Eqs. (B.2-B.3), we can compute $p_p(t)$, $T_p(t)$, $\alpha_p(t)$, $\dot{m}_{BR}(t)$ and $h_{BR}(t)$.

7.2 Containment TH model(s)

Two different TH models are adopted: a per-ignition TH model that simulates the CB between $t = 0$ and $t = t_{ign}$ (described in Section 7.2.1), and a post-ignition TH models that simulates the CB between $t = t_{ign}$ and $t = T_m$ (described in Section 7.2.2). Both the TH models adopt a control volume approach, where the (non-deformable) control volume boundary coincides with the inner steel containment (Figure 4) having a volume V_{CB}. The thermodynamic system of interest consists of the mass of non-condensable gasses in the CB, m_{nc}, the mass of water vapour in the CB, m_v and the mass of liquid water in the containment room for leakage collection, m_l.

7.2.1 Containment TH pre-ignition model

For the pre-ignition TH model we assume: 1) m_l in saturation conditions, 2) m_v and m_{nc} in thermal equilibrium ($T_v = T_{nc} \equiv T_{cont}$), 3) the relative humidity in the containment equal to $\phi = 100\%$ (i.e., the vapor partial pressure p_v equal to the water saturation pressure at T_{cont}, i.e., $p_v = p_{v,sat}(T_{cont})$), 4) the air partial pressure computed by the perfect gas law.

We assume the total volume of the system is given by the sum of the volumes occupied by m_l, and m_{nc}:

$$V_{CB} = m_l v_l + \frac{m_{nc} R_{nc} T_{cont}}{p_{cont} - p_v} \tag{B.13}$$

where v_l is the specific volume of m_l that, in saturation conditions, depends only on the CB total pressure p_{cont} (i.e., $v_l = v_f(p_{cont})$), the quantity $\frac{R_{nc} T_{cont}}{p_{cont} - p_v}$ is the specific volume of non-condensable gases, and R_{nc} is the specific gas constant of non-condensable gasses, which is approximated as dry air (i.e., $R_{nc} = 287.0 \frac{J}{kg\,K}$).

The internal energy of the system is given by:

$$U = H - p_{cont} V_{CB} \tag{B.14}$$

where the total enthalpy of the system H is given by the sum of the enthalpies of m_l, m_v and m_{nc}:

$$H = m_l h_l + x m_{nc} h_v + m_{nc} h_{nc} \tag{B.15}$$

where x is the specific humidity defined as $x = m_v / m_{nc}$, h_l is the specific enthalpy of m_l, which depends only on the pressure (i.e., $h_l = h_f(p_{cont})$), h_v is the specific enthalpy of m_v, which is assumed equal to $h_v = r_0 + c_{p,v}(T_{cont} - T_0)$ (with $r_0 = 2500\ kJ/kg$, $c_{p,v} = 1.877\ kJ/(kg \cdot K)$, and $T_0 = 276.16\ K$) and h_{nc} is assumed equal to $h_{nc} = c_{p,nc}(T_{cont} - T_0)$, where the specific heat at constant pressure of non-condensable gases $c_{p,nc}$ is assumed equal to that of dry air (i.e., $c_{p,nc} = 1004.5\ J/(Kg \cdot K)$).

Considering that $p_v = \phi p_{v,sat}(T_{cont})$, x is a function of p_{cont} and T_{cont}:

$$x = \frac{m_v}{m_{nc}} = \frac{p_v V_{CB}/(R_v T_{cont})}{p_{nc} V_{CB}/(R_{nc} T_{cont})} = 0.622 \frac{\phi p_{v,sat}}{p_{cont} - \phi p_{v,sat}} \tag{B.16}$$

where $p_a = p_{cont} - p_v$ is the air partial pressure, and $R_v = 461.5 \frac{J}{kg\,K}$ and $R_a = 287.0 \frac{J}{kg\,K}$ are the specific gas constants of water vapour and air, respectively.

We can model the system by imposing the non-deformable condition for the control volume V_{CB}, the conservation of mass and the conservation of the energy:

$$\frac{d\left[m_l v_l + \frac{m_{nc} R_{nc} T_{cont}}{p_{cont} - p_v}\right]}{dt} = 0 \tag{B.17}$$

$$\dot{m}_l + \dot{x} m_{nc} = \dot{m}_{BR} + \dot{m}_{sp} \tag{B.18}$$

$$\dot{U} = \dot{m}_{BR} h_{f,p} + \dot{m}_{sp} h_{sp} + \dot{Q}_{DH} - \dot{Q}_{AW} \tag{B.19}$$

where $\dot{m}_{sp}$ and h_{sp} are the spray system water flow rate and enthalpy, respectively; $\dot{Q}_{DH}$ is the fraction of decay heat power released into the CB (assumed equal to 1% of the core nominal thermal power); $\dot{Q}_{AW}$ is the heat power released from the CB atmosphere to the CB steel wall.

By deriving Eq. (B.16) with respect to time and coupling it with Eqs. (B.17-B.19), we get a system of four differential equations in four unknowns (i.e., $m_l(t)$, $x(t)$, $p_{cont}(t)$ and $T_{cont}(t)$) which, after some manipulations, can be arranged in matrix form:

$$\begin{bmatrix} v_f & 0 & \left(m_l \frac{\partial v_f}{\partial p_{cont}} - \frac{m_{nc} R_{nc} T_{cont}}{(p_{cont}-p_v)^2}\right) & \left(\frac{m_{nc} R_{nc}}{p_{cont}-p_v} - \frac{m_{nc} R_{nc} T_{cont}}{(p_{cont}-p_v)^2}\frac{\partial p_v}{\partial T_{cont}}\right) \\ 0 & -1 & \left(-\frac{0.622\, p_v}{(p_{cont}-p_v)^2}\right) & \left(\frac{0.622\, p_{cont}}{(p_{cont}-p_v)^2}\frac{\partial p_v}{\partial T_{cont}} + \frac{0.622}{(p_{cont}-p_v)}\frac{\partial p_v}{\partial T_{cont}}\right) \\ 1 & m_{nc} & 0 & 0 \\ h_f & m_{nc}(r_0 + c_{p,v}(T_{cont} - T\_0)) & \left(m_l \frac{\partial h_f}{\partial p_{cont}} - V_{CB}\right) & \left(m_{nc}(c_{p,nc} + x c_{p,v})\right) \end{bmatrix} \begin{bmatrix} \dot{m}_l \\ \dot{x} \\ \dot{p}_{cont} \\ \dot{T}_{cont} \end{bmatrix} = \begin{bmatrix} 0 \\ 0 \\ \dot{m}_{BR} + \dot{m}_{sp} \\ \dot{m}_{BR} h_{BR} + \dot{m}_{sp} h_{sp} + \dot{Q}_{DH} - \dot{Q}_{AW} \end{bmatrix} \quad \text{(B.20)}$$

The heat power released from the CB atmosphere to the CB steel wall $\dot{Q}_{AW}$ is computed as:

$$\dot{Q}_{AW} = A_{AW} \alpha_{AW} (T_{cont} - T_w) \quad \text{(B.21)}$$

where A_{AW} is assumed equal to the total surface area of the steel containment (Table 3), $\alpha_{AW} = 300 \frac{W}{m^2 K}$ is the heat transfer coefficient between the CB atmosphere and the wall [60], and T_w is the steel containment wall temperature modeled through the following energy balance:

$$C_w \frac{dT_W}{dt} = A_{AW} \alpha_{AW} (T_{cont} - T_w) - \dot{Q}_{ext} \quad \text{(B.22)}$$

where C_w is the heat capacity of the steel containment and $\dot{Q}_{ext}$ is the heat power released to the environment, computed as:

$$\dot{Q}_{ext} = (R_{23} + R_{34} + R_{ext})(T_w - T_{ext}) \quad \text{(B.23)}$$

where T_{ext} is the external temperature and R_{23}, R_{34}, R_{ext} are thermal resistances, whose subscripts refer to the CB structures indicated in Figure 14:

$$R_{23} = \frac{r_3 - r_2}{4\pi r_3 r_2 k_{eff}} \quad \text{(B.24)}$$

$$R_{34} = \frac{r_4 - r_3}{4\pi r_4 r_3 k_c} \quad \text{(B.25)}$$

$$R_{ext} = \frac{1}{4\pi r_{ext}^2 \alpha_{ext}} \quad \text{(B.26)}$$

k_{eff} is the effective thermal conductivity in the gap between the steel and concrete containment computed following [61], k_c is the concrete thermal conductivity and α_{ext} is the heat transfer coefficient on the external surface of the concrete CB, assumed equal to $\alpha_{ext} = 10 \frac{W}{m^2 K}$.

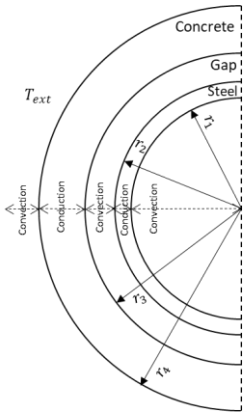

Figure 14. Heat transfer process in the containment.

The water vapour molar fraction X_{H2O} and hydrogen molar fraction X_{H2} are computed as:

$$X_{H2O} = \frac{n_{H2O}}{n_{nc} + n_{H2O} + n_{H2}} \tag{B.27}$$

$$X_{H2} = \frac{n_{H2}}{n_{nc} + n_{H2O} + n_{H2}} \tag{B.28}$$

n_{nc} is the number of $kmol$ of non-condensable gases (assumed to be composed for the $21\%_{v/v}$ by O_2 and for the remaining $79\%_{v/v}$ by N_2), computed through the ideal gas law:

$$n_{nc} = \frac{\left[p_{cont,0} - p_{v,sat}(T_{cont,0})\right]V_{CB}}{R_{nc} \cdot (273.15 + T_{cont,0})} \tag{B.29}$$

where $p_{cont,0}$ and $T_{cont,0}$ are the initial pressure and temperature in the CB and $R = 8314\,\frac{J}{kmol\,K}$ is the ideal gas constant.

n_{H2O} is the number of water vapour $kmol$ in the CB, computed as:

$$n_{H2O} = \frac{x m_{nc}}{M_{H2O}} \tag{B.30}$$

where $M_{H2O} = 18\,\frac{kg}{kmol}$ is the water molecular mass.

n_{H2} is the number of hydrogen $kmol$ in the CB, computed as:

$$n_{H2} = \frac{PR_{H_2} \cdot t}{M_{H2}} \tag{B.31}$$

where $M_{H2} = 2\,\frac{kg}{kmol}$ is the hydrogen molecular mass.

At the beginning of the accident, we assume $p_{cont,0} = 1\ Bar$, $T_{cont,0} = 50\ °C$ and $m_{l,0} = 0\ kg$, whereas x_0 is computed applying (B.16) by assuming $\phi_0 = 60\%$.

7.2.2 Containment TH post-ignition model

If $C_{regime}(t_{ign}) > 0$: i) the Simulink simulation with the TH pre-ignition model stops in $t = t_{ign}$; ii) the static pressure load on the CB resulting from hydrogen combustion $p_{eq,static}$ is computed [44]; iii) the CB hydrogen-air mixture conditions right after the combustion (i.e., $p_{cont}(t_{ign} + \Delta t)$, $T_{cont}(t_{ign} + \Delta t)$, $X_{H2O}(t_{ign} + \Delta t)$ and $X_{H2}(t_{ign} + \Delta t)$) are calculated and set as initial conditions for the Simulink TH post-ignition model that completes the simulation between $t_{ign} + \Delta t$ and T_m. In this Appendix, we do not show the procedure adopted for the computation of the CB hydrogen-air mixture conditions right after the combustion, which are then set as initial conditions for the Simulink TH post-ignition model.

In the containment TH post-ignition model, it is assumed that m_v can exist either under saturation conditions (i.e., $p_v = p_{v,sat}(T_{cont})$), and in that case the containment TH pre-ignition and post-ignition models coincides, or under unsaturated conditions (i.e., $p_v < p_{v,sat}(T_{cont})$), and in that case the two models differ. This assumption stems from the significant heat released during hydrogen combustion, which can lead to the complete evaporation of m_l and a substantial increase in T_{cont} within the CB. As a result, the air mixture may still be capable of holding additional water vapor before condensation begins (i.e., $p_v < p_{v,sat}(T_{cont})$). Thus, in the containment TH post-ignition model p_v is estimated at every t using the perfect gas law:

$$p_v(t) = \frac{x(t) m_{nc} R_v T_{cont}(t)}{V_{CB}} \tag{B.32}$$

then, if $p_v \geq p_{v,sat}(T_{cont})$, p_v is set equal to $p_{v,sat}(T_{cont})$ and the same TH model used for the pre-ignition (see Section 7.2.1) is adopted.

Conversely, if $p_v < p_{v,sat}(T_{cont})$:

- it is assumed that all liquid water is evaporated (i.e., $m_l = 0$); thus, the conservation of the mass is written as:

$$\dot{x} m_{nc} = \dot{m}_{BR} + \dot{m}_{sp} \tag{B.33}$$

and no water vapour condensation occurs:

$$\dot{m}_l = 0 \tag{B.34}$$

- The total pressure in the CB is given by the sum of the non-condensable gases partial pressure p_{nc} and the water vapour partial pressure p_v:

$$p_{cont} = p_{nc} + p_v \tag{B.35}$$

where $p_{nc} = \frac{m_{nc} R_{nc} T_{cont}}{V_{CB}}$ and $p_v = \frac{x m_{nc} R_v T_{cont}}{V_{CB}}$.

- The conservation of the energy is given by

$$\frac{d[H - p_{cont}V_{CB}]}{dt} = \dot{m}_{BR}h_{f,p} + \dot{m}_{sp}h_{sp} + \dot{Q}_{DH} - \dot{Q}_{AW} \tag{B.36}$$

where the total enthalpy of the system is $H = xm_{nc}h_v + m_{nc}h_{nc}$, and h_v and h_{nc} are computed as in Section 7.2.1.

By deriving Eq. (B.35) with respect to time and considering the conservation of the volume (i.e., $\dot{V_{CB}} = 0$) in Eq. (B.36), Eqs. (B.33-B.36) can be written, after some manipulations, in matrix form:

$$\begin{bmatrix} 0 & \frac{R_v m_{nc} T_{cont}}{V_{CB}} & -1 & \left(\frac{m_{nc}R_{nc}}{V_{CB}} + \frac{x m_{nc}R_v}{V_{CB}}\right) \\ 0 & m_{nc} & 0 & 0 \\ 1 & 0 & 0 & 0 \\ 0 & m_{nc}(r_0 + c_{p,v}(T_{cont} - T\_0)) & -V_{CB} & \left(m_{nc}(c_{p,nc} + xc_{p,v})\right) \end{bmatrix} \begin{bmatrix} \dot{m}_l \\ \dot{x} \\ \dot{p}_{cont} \\ \dot{T}_{cont} \end{bmatrix} = \begin{bmatrix} 0 \\ \dot{m}_{BR} + \dot{m}_{sp} \\ 0 \\ \dot{m}_{BR}h_{BR} + \dot{m}_{sp}h_{sp} + \dot{Q}_{DH} - \dot{Q}_{AW} \end{bmatrix} \tag{B.37}$$

If, for any reason $p_v \geq p_{v,sat}(T_{cont})$ holds again, the CB switches back to the Containment TH pre-ignition model.

The computation of $\dot{Q}_{AW}$, X_{H2O} and X_{H2} is carried out as for Section 7.2.1.

8 Appendix C

Table 16. DBN structure summary: node symbols, descriptions, types, and their parent–child dependencies across static and dynamic variables.

Symbol	Description	Type	Parents	Children
Ψ_{POC}	Initial plant operating conditions	Static hidden	–	Ψ_{IE}, ϕ_{pP0}, ϕ_{pT0}
Ψ_{IE}	Initiating event	Static hidden	Ψ_{POC}	$\Psi_{r_{BS}}$, $\Psi_{PR_{H_2}}$
ϕ_{pP0}	Primary circuit initial pressure	Static observable	Ψ_{POC}	$Y_{p_{cont(k)}}$,$Y_{T_{cont(k)}}$ for $k = 0, \dots, T$
ϕ_{pT0}	Primary circuit initial temperature	Static observable	Ψ_{POC}	$Y_{p_{cont(k)}}$,$Y_{T_{cont(k)}}$ for $k = 0, \dots, T$
$\Psi_{r_{BS}}$	Break size on the primary circuit	Static hidden	Ψ_{IE}	$Y_{p_{cont(k)}}$,$Y_{T_{cont(k)}}$, $Y_{X_{H2O(k)}}$,$Y_{X_{H2(k)}}$ for $k = 0, \dots, T$

Symbol	Description	Type	Parents	Children
$\Psi_{PR_{H_2}}$	Hydrogen production rate	Static hidden	Ψ_{IE}	$Y_{p_{cont(k)}}, Y_{T_{cont(k)}}$, $Y_{X_{H2O(k)}}, Y_{X_{H2(k)}}$, for $k = 0, \dots, T$
$Y_{p_{cont(k)}}$	CB pressure	Dynamic observable	$\phi_{pP0}, \phi_{pT0}, \Psi_{r_{BS}}$, $\Psi_{PR_{H_2}}, Y_{sp_{(k-1)}}$, $Y_{p_{cont(k-1)}}$	$X_{CB_{DS}(k)}, X_{C_{reg}(k)}$, $Y_{sp(k)}, Y_{X_{H2O(k)}}, Y_{X_{H2(k)}}$, $Y_{p_{cont(k+1)}}$
$Y_{T_{cont(k)}}$	CB temperature	Dynamic observable	$\phi_{pP0}, \phi_{pT0}, \Psi_{r_{BS}}$, $\Psi_{PR_{H_2}}, Y_{sp_{(k-1)}}$, $Y_{T_{cont(k-1)}}$	$Y_{X_{H2O(k)}}, Y_{X_{H2(k)}}$, $X_{C_{reg}(k)}, Y_{T_{cont(k+1)}}$
$Y_{X_{H2O(k)}}$	Steam molar fraction in the CB	Dynamic observable	$\Psi_{r_{BS}}, \Psi_{PR_{H_2}}, Y_{T_{cont(k)}}$, $Y_{p_{cont(k)}}, Y_{X_{H2O(k-1)}}$	$X_{C_{reg}(k)}, Y_{X_{H2O(k+1)}}$
$Y_{X_{H2(k)}}$	Hydrogen molar fraction in the CB	Dynamic observable	$\Psi_{r_{BS}}, \Psi_{PR_{H_2}}, Y_{T_{cont(k)}}$, $Y_{p_{cont(k)}}, Y_{X_{H2(k-1)}}$	$X_{C_{reg}(k)}, Y_{X_{H2(k+1)}}$
$X_{C_{reg}(k)}$	Combustion regime in the CB	Dynamic hidden	$Y_{X_{H2O(k)}}, Y_{X_{H2(k)}}$, $Y_{p_{cont(k)}}, Y_{T_{cont(k)}}$	–
$A_{sp_{(k)}}$	Operator action on spray system	Dynamic action node	–	$Y_{sp_{(k)}}$
$Y_{sp_{(k)}}$	Spray system operational state	Dynamic observable	$A_{sp_{(k)}}, Y_{p_{cont(k)}}$	$Y_{p_{cont(k+1)}}, Y_{T_{cont(k+1)}}$
$X_{CB_{DS}(k)}$	CB damage state	Dynamic hidden	$Y_{p_{cont(k)}}, X_{CB_{DS}(k-1)}$	$X_{CB_{DS}(k+1)}$

References

[1] AGENCY IAE. Accident management programmes for nuclear power plants. Specific Safety Guide SSG-54. Safety Guide 2019:83.

[2] Zhao N, Ma W, Bechta S. A review of the assessment of severe accident management guidelines and actions through analytical simulations. Ann Nucl Energy 2023;180:109448. https://doi.org/https://doi.org/10.1016/j.anucene.2022.109448.

[3] Zavisca MJ, Khatib-Rahbar M, Esmaili H, Schulz R. Adam: An accident diagnostic, analysis and management system - Applications to severe accident simulation and management. International Conference on Nuclear Engineering, Proceedings, ICONE, vol. 2, 2002, p. 131 – 136. https://doi.org/10.1115/ICONE10-22195.

[4] Øwre F. Role of the man–machine interface in accident management strategies. Nuclear Engineering and Design 2001;209:201–10. https://doi.org/https://doi.org/10.1016/S0029-5493(01)00403-4.

[5] Khatib-Rahbar M, Zavisca M, Esmaili H, Cazzoli EG, Schmocker U, Schoen G, et al. Accident diagnostic, analysis and management (ADAM) system applications to severe accident management. OECD Workshop on operator training for Severe Accident Management and Instrumentation Capabilities during Severe Accidents, 2001.

[6] Silverman EB. SAMSON: Severe accident management system on-line network. International Atomic Energy Agency (IAEA): 1994.

[7] Saghafi M, Ghofrani MB. Accident management support tools in nuclear power plants: A post-Fukushima review. Progress in Nuclear Energy 2016;92:1–14. https://doi.org/https://doi.org/10.1016/j.pnucene.2016.06.006.

[8] Zio E, Gola G. Neuro-fuzzy pattern classification for fault diagnosis in nuclear components. Ann Nucl Energy 2006;33:415–26. https://doi.org/10.1016/j.anucene.2005.12.008.

[9] Darling MC, Luger GF, Jones TB, Denman MR, Groth KM. Intelligent Modeling for Nuclear Power Plant Accident Management. International Journal on Artificial Intelligence Tools 2018;27:1850003. https://doi.org/10.1142/S0218213018500033.

[10] Groth KM, Denman MR, Darling MC, Jones TB, Luger GF. Building and using dynamic risk-informed diagnosis procedures for complex system accidents. Proc Inst Mech Eng O J Risk Reliab 2020;234:193–207. https://doi.org/10.1177/1748006X18803836.

[11] Roma G, Maio F Di, Zio E. A condition-informed dynamic Bayesian network framework to support severe accident management in nuclear power plants. Reliab Eng Syst Saf 2024;252:110437. https://doi.org/https://doi.org/10.1016/j.ress.2024.110437.

[12] KIM J, ZHAO X, SHAH AUA, KANG HG. System risk quantification and decision making support using functional modeling and dynamic Bayesian network. Reliab Eng Syst Saf 2021;215:107880. https://doi.org/https://doi.org/10.1016/j.ress.2021.107880.

[13] Kim J, Shah AUA, Kang HG. Dynamic risk assessment with bayesian network and clustering analysis. Reliab Eng Syst Saf 2020;201:106959. https://doi.org/https://doi.org/10.1016/j.ress.2020.106959.

[14] Oliphant TA, Witte KH. RAVEN. United States: 1987.

[15] Tosoni E, Salo A, Govaerts J, Zio E. Comprehensiveness of scenarios in the safety assessment of nuclear waste repositories. Reliab Eng Syst Saf 2019;188:561–73. https://doi.org/10.1016/j.ress.2019.04.012.

[16] Tolo S, Patelli E, Beer M. An open toolbox for the reduction, inference computation and sensitivity analysis of Credal Networks. Advances in Engineering Software 2018;115:126–48. https://doi.org/https://doi.org/10.1016/j.advengsoft.2017.09.003.

[17] Jae M, Moon JH. Use of a fuzzy decision-making method in evaluating severe accident management strategies. Ann Nucl Energy 2002;29:1597–606. https://doi.org/https://doi.org/10.1016/S0306-4549(01)00125-6.

[18] Cozman FG. Credal networks. Artif Intell 2000;120:199–233. https://doi.org/https://doi.org/10.1016/S0004-3702(00)00029-1.

[19] Morais C, Estrada-Lugo HD, Tolo S, Jacques T, Moura R, Beer M, et al. Robust data-driven human reliability analysis using credal networks. Reliab Eng Syst Saf 2022;218:107990. https://doi.org/https://doi.org/10.1016/j.ress.2021.107990.

[20] Alonso-Martín P-R, Montes I, Miranda E. Distortion models for estimating human error probabilities. Saf Sci 2023;157:105915. https://doi.org/https://doi.org/10.1016/j.ssci.2022.105915.

[21] Hruschka Estevam R. and Hruschka ER and ENFF. Feature Selection by Bayesian Networks. In: Tawfik Ahmed Y. and Goodwin SD, editor. Advances in Artificial Intelligence, Berlin, Heidelberg: Springer Berlin Heidelberg; 2004, p. 370–9.

[22] Cinicioglu EN, Shenoy PP. A new heuristic for learning Bayesian networks from limited datasets: a real-time recommendation system application with RFID systems in grocery stores. Ann Oper Res 2016;244:385–405. https://doi.org/10.1007/s10479-012-1171-9.

[23] Hamza Z, Abdallah T. Mapping Fault Tree into Bayesian Network in safety analysis of process system. 2015 4th International Conference on Electrical Engineering (ICEE), 2015, p. 1–5. https://doi.org/10.1109/INTEE.2015.7416862.

[24] Khakzad N, Khan F, Amyotte P. Dynamic safety analysis of process systems by mapping bow-tie into Bayesian network. Process Safety and Environmental Protection 2013;91:46–53. https://doi.org/10.1016/j.psep.2012.01.005.

[25] Wu X, Huang H, Xie J, Lu M, Wang S, Li W, et al. A novel dynamic risk assessment method for the petrochemical industry using bow-tie analysis and Bayesian network analysis method based on the

methodological framework of ARAMIS project. Reliab Eng Syst Saf 2023;237:109397. https://doi.org/https://doi.org/10.1016/j.ress.2023.109397.

[26] Koller D, Friedman N. Probabilistic Graphical Models: Principles and Techniques - Adaptive Computation and Machine Learning. The MIT Press; 2009.

[27] Mkrtchyan L, Podofillini L, Dang VN. Methods for building Conditional Probability Tables of Bayesian Belief Networks from limited judgment: An evaluation for Human Reliability Application. Reliab Eng Syst Saf 2016;151:93–112. https://doi.org/https://doi.org/10.1016/j.ress.2016.01.004.

[28] Murphy KP, Russell SJ. Dynamic bayesian networks: representation, inference and learning, 2002.

[29] Podofillini L, Reer B, Dang VN. A traceable process to develop Bayesian networks from scarce data and expert judgment: A human reliability analysis application. Reliab Eng Syst Saf 2023;230:108903. https://doi.org/https://doi.org/10.1016/j.ress.2022.108903.

[30] A. FN, Qian SS, Stow CA. Comparative analysis of discretization methods in Bayesian networks. Environmental Modelling & Software 2017;87:64–71. https://doi.org/https://doi.org/10.1016/j.envsoft.2016.10.007.

[31] Zhu J, Collette M. A dynamic discretization method for reliability inference in Dynamic Bayesian Networks. Reliab Eng Syst Saf 2015;138:242–52. https://doi.org/https://doi.org/10.1016/j.ress.2015.01.017.

[32] Lewis AD, Groth KM. A comparison of DBN model performance in SIPPRA health monitoring based on different data stream discretization methods. Reliab Eng Syst Saf 2023;236:109206. https://doi.org/https://doi.org/10.1016/j.ress.2023.109206.

[33] Casella G, Berger RL. Statistical Inference. 2nd ed. Pacific Grove, CA: Duxbury Press; 2002.

[34] Drouin M, Gilbertson A, Parry G, Lehner J, Martinez-Guridi G, LaChance J, et al. NUREG-1855, Revision 1: Guidance on the Treatment of Uncertainties Associated with PRAs in Risk-Informed Decisionmaking. 2017.

[35] Kang S, Yu J, Seong PH. Development of a decision-making support system for the technical support center based on analysis of human performance under severe accident situation. Ann Nucl Energy 2022;166:108702. https://doi.org/https://doi.org/10.1016/j.anucene.2021.108702.

[36] Chen S-H. Ranking fuzzy numbers with maximizing set and minimizing set. Fuzzy Sets Syst 1985;17:113–29. https://doi.org/https://doi.org/10.1016/0165-0114(85)90050-8.

[37] Kim K, Park KS. Ranking fuzzy numbers with index of optimism. Fuzzy Sets Syst 1990;35:143–50. https://doi.org/10.1016/0165-0114(90)90189-D.

[38] Liou T-S, Wang M-JJ. Ranking fuzzy numbers with integral value. Fuzzy Sets Syst 1992;50:247–55. https://doi.org/https://doi.org/10.1016/0165-0114(92)90223-Q.

[39] Noori-Kalkhoran O, Rahgoshay M, Minuchehr A, Shirani AS. Analysis of thermal–hydraulic parameters of WWER-1000 containment in a large break LOCA. Ann Nucl Energy 2014;68:101–11. https://doi.org/https://doi.org/10.1016/j.anucene.2014.01.009.

[40] Omidifard P, Pirouzmand A, Hadad K, Rezaee J. Investigating the effect of spray system on the containment condition of VVER1000/V446 NPP during LBLOCA and TLOFW accidents. Nuclear Engineering and Design 2023;413:112562. https://doi.org/https://doi.org/10.1016/j.nucengdes.2023.112562.

[41] Moody FJ. Maximum Flow Rate of a Single Component, Two-Phase Mixture. J Heat Transfer 1965;87:134–41. https://doi.org/10.1115/1.3689029.

[42] Martín-Valdepeñas JM, Jiménez MA, Martín-Fuertes F, Fernández JA. Corrigendum to "Improvements in a CFD code for analysis of hydrogen behaviour within containments" (Nucl. Eng. Design 237 (2007) (627–647) (S0029549306005048)(10.1016/j.nucengdes.2006.09.002)). Nuclear Engineering and Design 2017;311:224. https://doi.org/10.1016/j.nucengdes.2016.12.019.

[43] Martín-Valdepeñas JM, Jiménez MA, Martín-Fuertes F, Fernández JA. Improvements in a CFD code for analysis of hydrogen behaviour within containments. Nuclear Engineering and Design 2007;237:627–47. https://doi.org/10.1016/j.nucengdes.2006.09.002.

[44] Breitung W, Redlinger R. Model for structural response to hydrogen combustion loads in severe accidents. Nucl Technol 1995;111:420–5. https://doi.org/10.13182/NT95-A15870.

[45] https://www.bayesfusion.com/ n.d.

[46] Yuan C, Druzdzel MJ. An Importance Sampling Algorithm Based on Evidence Pre-propagation. CoRR 2012;abs/1212.2507.

[47] International Atomic Energy Agency. Mitigation of Hydrogen Hazards in Severe Accidents in Nuclear Power Plants. Vienna: 2011.

[48] NUREG/CR-5750, "Rates of Initiating Events at U.S. Nuclear Power Plants: 1987 - 1995." n.d.

[49] Guba A, Makai M, Pál L. Statistical aspects of best estimate method - I. Reliab Eng Syst Saf 2003;80:217–32. https://doi.org/10.1016/S0951-8320(03)00022-X.

[50] U.S. Nuclear Regulatory Commission. SECY-19-0047: Containment Performance Goals for the NuScale Small Modular Reactor Design. Washington, DC: 2019.

[51] Zwirglmaier K, Straub D. A discretization procedure for rare events in Bayesian networks. Reliab Eng Syst Saf 2016;153:96–109. https://doi.org/https://doi.org/10.1016/j.ress.2016.04.008.

[52] Wang L, Huang S, Wang S, Liao J, Li T, Liu L. A survey of causal discovery based on functional causal model. Eng Appl Artif Intell 2024;133:108258. https://doi.org/https://doi.org/10.1016/j.engappai.2024.108258.

[53] Liu W, Liu F, Fang W, Love PED. Causal discovery and reasoning for geotechnical risk analysis. Reliab Eng Syst Saf 2024;241:109659. https://doi.org/https://doi.org/10.1016/j.ress.2023.109659.

[54] Salmerón A, Rumí R, Langseth H, Nielsen TD, Madsen AL. A review of inference algorithms for hybrid Bayesian networks. Journal of Artificial Intelligence Research 2018;62:799–828. https://doi.org/10.1613/jair.1.11228.

[55] Bensi M, Kiureghian A Der, Straub D. Efficient Bayesian network modeling of systems. Reliab Eng Syst Saf 2013;112:200–13. https://doi.org/https://doi.org/10.1016/j.ress.2012.11.017.

[56] Rohmer J. Uncertainties in conditional probability tables of discrete Bayesian Belief Networks: A comprehensive review. Eng Appl Artif Intell 2020;88. https://doi.org/10.1016/j.engappai.2019.103384.

[57] Mauá DD, Cozman FG. Thirty years of credal networks: Specification, algorithms and complexity. International Journal of Approximate Reasoning 2020;126:133–57. https://doi.org/10.1016/j.ijar.2020.08.009.

[58] Polpo De Campos C, Cozman FG. The Inferential Complexity of Bayesian and Credal Networks. n.d.

[59] Heckerman D, Geiger D, Chickering DM. Learning Bayesian Networks: The Combination of Knowledge and Statistical Data. Mach Learn 1995;20:197–243. https://doi.org/10.1023/A:1022623210503.

[60] Martín-Valdepeñas JM, Jiménez MA, Martín-Fuertes F, Benítez JAF. Comparison of film condensation models in presence of non-condensable gases implemented in a CFD Code. Heat and Mass Transfer/Waerme- Und Stoffuebertragung 2005;41:961–76. https://doi.org/10.1007/s00231-004-0606-5.

[61] Raithby GD, Hollands KGT. A General Method of Obtaining Approximate Solutions to Laminar and Turbulent Free Convection Problems. In: Irvine TF, Hartnett JP, editors. vol. 11, Elsevier; 1975, p. 265–315. https://doi.org/https://doi.org/10.1016/S0065-2717(08)70076-5.